Plume-Induced Flood Basalts on Hesperian Mars: An Investigation of Hesperia Planum

Adrien Pierre Michel Broquet[1] and Jeffrey C. Andrews-Hanna[1]

[1]Lunar and Planetary Laboratory University of Arizona

November 26, 2022

Abstract

Hesperian Mars was characterized by a unique style of geodynamic activity that left crucial volcano-tectonic records in the form of extensive flood lavas covered by wrinkle ridges. Yet, little is known about the context of their formation. Here, we perform a tectonic and geophysical investigation of Hesperia Planum, a 1700-km-diameter volcanic plain covered by wrinkle ridges. Our tectonic analysis reveals that the planum has the highest density of wrinkle ridges on the planet and a characteristic compressional peak strain of about 3.20×10-3, almost 2 times larger than typical Hesperian compressional strains. We invert gravity and topography data and find that simple crustal loading and volcanism cannot explain the tectonic record. An additional source of deformation is thus required. We demonstrate that a loading sequence of plume-induced uplift, volcanism, and subsidence, following an evolutionary path similar to flood basalt provinces on Earth better fits the observations. This plume model is able to explain the peak strain, bottom loading (crustal thinning or density increase), and low relief of Hesperia Planum. The inferred plume head size (˜1400 km) and temperature anomaly (˜320 K) are consistent with large terrestrial plumes. Based on a fit to the tectonic record, we determine a plume center location that correlates with a cluster of wrinkle ridges, local bottom loading, and circular magnetic low, where the latter could be the result of a thermal demagnetization of the lithosphere in the presence of the ascending plume. Our analysis suggests that scattered Hesperian mantle plumes could be at the origin of the volcanic ridged plains.

Plume-Induced Flood Basalts on Hesperian Mars: An Investigation of Hesperia Planum

Broquet A.[1] and Andrews-Hanna J. C.[1]

[1]Lunar and Planetary Laboratory, University of Arizona, Tucson, AZ 85721, USA

Corresponding author: Adrien Broquet, abroquet@lpl.arizona.edu

Key Points:

- Hesperia Planum shows volcanism, compression, crustal demagnetization and thinning
- Compressional tectonics cannot be explained by global cooling or volcanic loading
- The planum is inferred to have formed as a terrestrial plume-induced flood basalt
- The formation sequence involves plume-induced uplift, volcanism, and subsidence
- Hesperian plumes likely formed ridged volcanic plains outside of the Tharsis province

Abstract:

Hesperian Mars was characterized by a unique style of geodynamic activity that left crucial volcano-tectonic records in the form of extensive flood lavas covered by wrinkle ridges. Yet, little is known about the context of their formation. Here, we perform a tectonic and geophysical investigation of Hesperia Planum, a 1700-km-diameter volcanic plain covered by wrinkle ridges. Our tectonic analysis reveals that the planum has the highest density of wrinkle ridges on the planet and a characteristic compressional peak strain of about 3.20×10^{-3}, almost 2 times larger than typical Hesperian compressional strains. We invert gravity and topography data and find that simple crustal loading and volcanism cannot explain the tectonic record. An additional source of deformation is thus required. We demonstrate that a loading sequence of plume-induced uplift, volcanism, and subsidence, following an evolutionary path similar to flood basalt provinces on Earth better fits the observations. This plume model is able to explain the peak strain, crustal thinning, and low relief of Hesperia Planum. The inferred plume head size (~1400 km) and temperature anomaly (~320 K) are consistent with large terrestrial plumes. Based on a fit to the tectonic record, we determine a plume center location that correlates with a cluster of wrinkle ridges, local crustal thinning, and a circular magnetic low, where the latter could be the result of a thermal demagnetization of the lithosphere in the presence of the ascending plume. Our analysis suggests that scattered mantle plumes could be at the origin of Hesperia Planum and other late Noachian to early Hesperian volcanic provinces within the highlands.

1 Introduction

Volcanic products are testimonies of a planet's internal activity and can be used to infer its geologic history (L. Wilson & Head, 1983; Greeley & Schneid, 1991). On Earth, surface manifestations of different aspects of mantle dynamics are found in the form of plate tectonics (T. J. Wilson, 1965) and the presence of plume-induced hotspots (Morgan, 1971) and large igneous provinces (Richards et al., 1989; Coffin & Eldholm, 1994). A large igneous province is commonly thought of as a vast ($>10^5$ km^2) and low-relief effusive intraplate volcanic deposit (Coffin and Eldholm, 1994; Ernst, 2014; Ernst et al. 2021), which was emplaced over a relatively short period of time (few tens of Myr, Richards et al., 1989). Tens of large igneous provinces and their associated flood basalts have been found all across the Earth and are thought to have formed throughout our planet's history (see Ernst & Buchan, 2001, for a review).

The formation of large igneous provinces entails upwelling and decompression melting of mantle material, but the driving force is at the center of lively controversies and debates (see Davies, 2000; Foulger, 2010, for a review). A dynamic scenario suggests that large igneous provinces and flood basalts are due to ascending plumes of anomalously hot material coming from the lower mantle (Richards et al., 1989; Griffiths & Campbell, 1991; Torsvik et al., 2010). Alternative scenarios do not necessarily require mantle plumes, and instead involve, for example, local mantle dynamics with upper-mantle sources intersecting regions of lithospheric stretching and thinning (e.g., Anderson, 2000; Hales et al., 2005).

Flood basalt volcanism is common to all terrestrial planets (Head & Coffin, 1997). However, the flood volcanism on the Moon responsible for the nearside maria is linked to regions of thin crust and high concentrations of heat producing elements, and thus is not analogous to terrestrial large igneous provinces. Similarly, volcanism on Mercury is strongly concentrated in the enigmatic northern volcanic province. The planet's relatively thin mantle would hinder the formation of large mantle plumes as understood on Earth (Campbell & Griffiths 1990). For those reasons, the formation of the largest volcanic provinces on the Moon and Mercury are not likely to be associated with mantle plumes as traditionally viewed on Earth.

Venus harbors several large volcanic provinces with radiating dike structure resembling the large igneous provinces found on Earth (e.g., Head & Coffin, 1997; Ernst & Desnoyer 2004; Hansen 2007; MacLellan et al., 2021). Mars is a basalt-covered world, with about 40% of the planet's surface being covered by lava flows of Hesperian age (3.7–3.4 Ga, Tanaka et al., 2014). However, the large Tharsis volcanic rise and the vast volcanic plains covering the northern lowlands are unlike large igneous provinces on Earth in scale (~10^7 versus 10^5 km^2) and evolutionary history, and may be related to hemisphere-scale mantle upwellings (e.g., Redmond & King, 2004). In contrast, the southern highlands harbor several discrete late Noachian and early Hesperian volcanic plains covered by wrinkle ridges that are similar in scale to large igneous provinces on Earth. The high eruption rate that characterized this plains-forming volcanism is further reminiscent of that in plume-induced flood basalts and large igneous provinces on Earth (e.g., Head & Coffin,

1997; Mège & Ernst, 2001; Head et al., 2006). Mars has spent most, if not all, of its evolutionary path in a stagnant lid regime without plate tectonics (Solomon, 1978), and with minimal surface erosion for the past 3.5 Gyr. For that reason, the planet holds a more pristine record of its geologic history than the Earth, including that of the formation and evolution of its volcanic provinces. Geologic and geophysical observations on Mars could thus be used to reveal the details of the formation of these provinces, thereby shedding light on the influence of mantle dynamics on magmatism. Although the unprecedented volcano-tectonic activity recorded on the Noachian-Hesperian wrinkle ridged plains may provide the best analogs to large igneous provinces on Earth, the predictions of the mantle plume hypothesis have not yet been explicitly tested against the available geophysical data.

In this study, we perform a tectonic and geophysical investigation of Hesperia Planum, a 1700 km-diameter volcanic plain covered by wrinkle ridges located in the southern hemisphere of Mars. This planum shares similarities to some terrestrial flood basalts and has the highest density of wrinkle ridges on the planet. We start by presenting the general geologic characteristics of the Noachian-Hesperian ridged plains on Mars and how they compare to terrestrial flood basalt provinces. Next, we discuss the topography, gravity, magnetic, and tectonic data at Hesperia Planum. We then present our geophysical approach to determine how the planum formed, including gravity and topography analyses, and a comparison of the tectonic strain

to predictions of a mantle plume model. In the last section, we discuss the implications of our results for the formation of Hesperia Planum.

2 Background and previous work

2.1 Noachian-Hesperian ridged plains

The southern highlands of Mars harbors two large early Hesperian volcanic ridged plains near the Hellas impact basin (Tanaka et al., 2014), namely Syrtis Major (10°N, 60°E) and Hesperia Plana (20°S, 105°E), which have diameters of 1400 to 1700 km (Figure 1). A third major ridged plain, Malea Planum (65°S, 60°E) is located south of Hellas and displays similar overall characteristics as the Hesperian ridged plains, though is slightly older with a Late Noachian age (3.84–3.7 Ga; Tanaka et al., 2014). In the western hemisphere Hesperian lava plains occur within Tharsis, such as Syria and Lunae Plana (Scott & Tanaka, 1986; Golombek & Phillips, 2009). Hesperian ridged plains also cover the northern lowlands, beneath a thin sedimentary layer (Head et al., 2002). However, the Noachian-Hesperian highland volcanic provinces (Hesperia, Syrtis Major, and Malea Plana) formed over relatively short time spans (<200 Myr, Williams et al. 2010; Robbins et al. 2011) with little to no subsequent plains-forming volcanism. This high volcanic pulse makes them distinct from the ridged volcanic plains within Tharsis and covering the northern lowlands that display a more steady volcanic history unique to those particular settings. In this work, we focus on the Noachian-Hesperian highland volcanic provinces (Hesperia, Syrtis Major,

and Malea Plana, with Hesperia Planum taken as the archetype) as potential analogs to continental flood basalt provinces on Earth (Head & Coffin, 1997).

The Noachian-Hesperian highland volcanic provinces sit in subtle 1 to 1.5 km depressions with respect to the surrounding highlands (Figure 1). Such depressions cannot be explained by the flexural response to surface volcanic loading only, as this would not push the volcanic surface below the pre-existing surface. An additional source of crustal modification is thus required to form these ridged plains beyond the observed volcanism alone. These volcanic provinces are further characterized by smooth lava flows with a high density of long (tens to hundreds of km) and sinuous wrinkle ridges (Knapmeyer et al., 2006), which form by folding of near-surface layered volcanic flows above blind thrust faults (Schultz, 2000). The orientation of the ridges as well as the associated strain are related to loading and deformation of the lithosphere and provide important clues on the geodynamic context of their formation (e.g., Mège & Ernst, 2001; Montési & Zuber, 2003; Golombek & Phillips, 2009; Bethell et al., 2021).

The large concentration of wrinkle ridges on the Noachian-Hesperian highland volcanic provinces contrasts with tectonic features observed in the volcanic shields of the Tharsis province. The Tharsis Montes are associated with enormous compressional flexural strain (Banerdt et al., 1982), but little to no compressional tectonics (Golombek & Phillips, 2009). This observation can be explained by a long history in which loading is in equilibrium with flexure, and where the uppermost layers corresponding to the latest eruption phase are close to strain-free. In

comparison, the high density of wrinkle ridges on the Noachian-Hesperian highland volcanic provinces would require a shorter burst of volcanism with flexural deformation following the eruption, rather than volcanism and flexure operating in parallel.

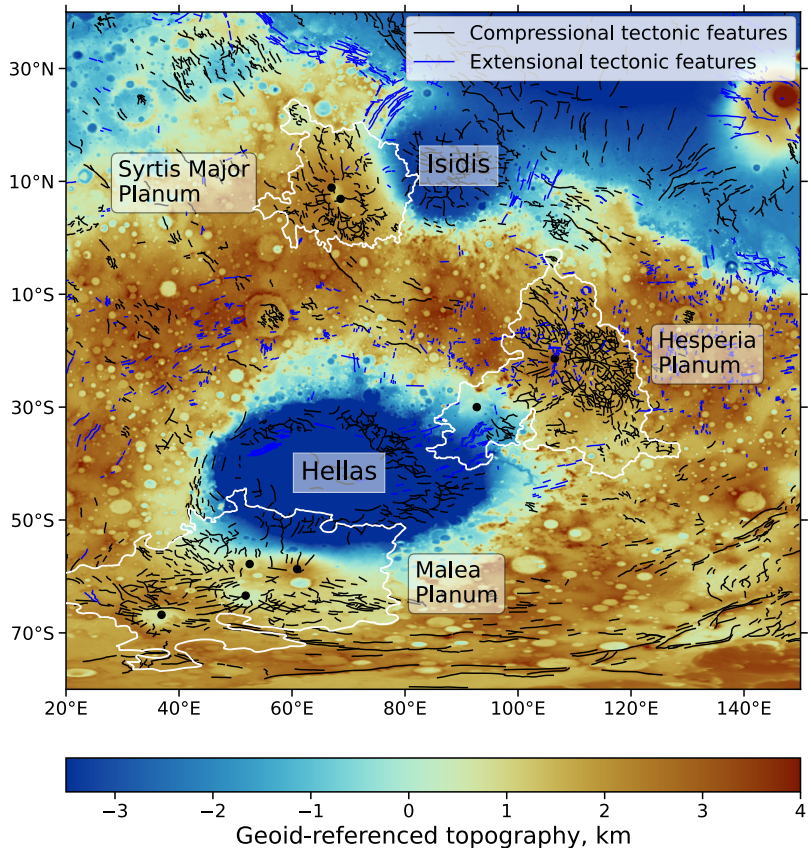

Figure 1 Surface elevations of the Hellas region. Three major volcanic units are displayed in white, including Syrtis Major, Hesperia, and Malea Plana (Tanaka et al., 2014). Two large impact basins, Isidis and Hellas are also referenced. Tensile structures (blue) and compressive features (black) as mapped by Knapmeyer et al. (2006) are annotated. Black dots indicate the positions of volcanic edifices, including Nili (67.0°E, 8.9°N), Meroe (68.6°E, 6.9°N), Tyrrhena (106.5°E, -21.4°N), Hadriaca (92.7°E, -30.0°N), Peneus (52.5°E, -57.8°N), Amphitrites (60.9°E, -58.7°N), Malea (51.8°E, -63.4°N), and Pityusa (36.9°E, -66.8°N) Montes. Topography data (Smith et al., 2001) are referenced to the geoid (Genova et al., 2016).

164
165 ### 2.2 A comparison with terrestrial flood basalts

166 The most pristine flood basalt province on Earth is the 800-km diameter, young
167 (~17 Ma), Columbia River Basalt Group in western North America (see Reidel et al.,
168 2013, for a review). The cause of the flood-basalt volcanism has been controversial
169 (e.g., Hales et al., 2005; Hooper et al., 2007), but a plume origin has been found to
170 best explain the geophysical and geochemical characteristics of the province (see
171 Camp, 2013, for a review). The Columbia River Basalt Group shares interesting
172 similarities with the Noachian-Hesperian ridged plains on Mars, including that it also
173 sits in a kilometer-scale broad depression, displays a local crustal thinning (Laske et
174 al., 2013), and is the only place on Earth in which wrinkle ridge-like thrust faulting
175 has been documented (Hooper & Conrey, 1989; Watters, 1989; Mège & Ernst, 2001).
176 These features are testimonies of regional subsidence of the plateau, which is thought
177 to be correlated with the rate of volcanic eruption (Reidel et al., 1989, 2013), and could
178 be linked to the deflation of the plume source. Furthermore, whereas typical plume-
179 induced flood basalts on Earth led to rifting and often transitioned to seafloor
180 spreading and ocean opening (Courtillot et al., 1999), the Columbia River Basalt
181 Group has not reached this final stage and is thus only moderately affected by plate
182 tectonics. One main difference between the Noachian-Hesperian highland volcanic
183 provinces and the Columbia River and other flood basalts on Earth is the overall
184 absence of major dike structures on the former, which are often associated with the
185 effects of mantle plumes (e.g., Ernst & Buchan, 2001). Some local dike systems have

186 been observed at Hadriaca Mons (Korteniemi et al., 2010), and western Terra
187 Tyrrhena (Head et al., 2006), but these are significantly smaller than the large
188 Mackenzie dike swarm in Canada with radiating dikes up to 3000 km long, or the
189 Chief Joseph dike swarm in the Columbia Plateau (Mège & Ernst, 2001; Buchan &
190 Ernst 2021). Radiating dike swarms require a horizontally extensional stress regime,
191 which may not have existed on Hesperian Mars away from the Tharsis volcanic rise.
192 This suggests that if large dike systems existed on the Noachian-Hesperian highland
193 volcanic provinces, they have been confined to the area of the plains and buried
194 beneath voluminous flood basalts.

195 These overall similarities allow us to suggest that the Noachian-Hesperian ridged
196 plains on Mars could have formed following an evolutionary path similar to large
197 igneous provinces on Earth, and we will here focus on the plume hypothesis. The
198 formation and evolution of a mantle plume is controlled by the thermophysical
199 characteristics of the lithosphere and mantle (Campbell & Griffiths 1990). Earth and
200 Mars are different in many respects, and this affects the generation of mantle plumes.
201 The dimensions of the plume head are primarily controlled by the height of rise
202 through the mantle, gravity, and viscosity of the mantle. Using scaling relationships
203 based on laboratory experiments (Campbell and Griffiths, 1990), it is possible to show
204 that for similar viscosities, the diameter of a plume head on Mars would be only about
205 15% smaller than on Earth, since the effects of gravity and rise height (mantle
206 thickness) partially cancel one another out. If instead the martian mantle viscosity
207 were two orders of magnitude different, the diameter would be 0.3 to 2 times larger

on Mars, where higher viscosities lead to larger plume heads (Text S1). This scaling suggests that similar plume head geometries could be found on Earth and Mars.

2.3 An idealized sequence of plume-induced flood basalt volcanism on a one-plate planet

The origin of large igneous provinces on Earth is still debated, with decompression melting being related to either plate tectonic processes or to the ascent of a deep mantle plume (see Davies, 2000; Foulger, 2010, for a review). For example, the North Atlantic Igneous Province is thought to have formed following rifting-induced delamination (Petersen et al., 2018), while the Columbia River Basalt Group may have formed from a deep mantle plume (Camp, 2013). Without plate tectonics on Mars, non-plume alternatives for the generation of volcanism involve passive scenarios such as partial melting below a thickened crust and melting due to small-scale mantle convection (or edge-driven convection), as well as active mechanisms such as eruption enabled by lithospheric extension and delamination. Eruptions driven by extension are incompatible with the dominantly compressional stress regime away from Tharsis during the Hesperian and the absence of regional extension associated with the Noachian-Hesperian ridged plains (Figure 1). All these mechanisms for generating volcanism would also not generate sufficient, if any, surface uplift and subsidence to explain the tectonic record as discussed below.

While plate tectonics may interact with plumes in the formation of large igneous provinces on Earth, the absence of global plate motions does not preclude the formation of plume-induced flood basalts, as widely inferred to be the case on Venus (e.g., Gülcher et al., 2020). For that reason, although significant uncertainties exist in the formation of large igneous provinces and their flood basalts on Earth, we here present an idealized plume-induced evolution sequence on a stagnant lid planet drawing from models and observations on the Earth (Figure 2). 1) A deep thermal anomaly creates a buoyant mantle plume that rises and causes thermal uplift and extension of the surface (e.g., Griffiths & Campbell, 1991; Farnetani & Richards, 1994; Rainbird & Ernst, 2001; Saunders et al., 2007). 2) The plume head impinges the base of the lithosphere and flattens, at which point thermal uplift is at a maximum (Griffiths & Campbell, 1991; Campbell, 2007) and crustal materials are replaced by plume materials causing a local crustal thinning (White & McKenzie, 1989). 3) Extensive flood basalts extrude through the thinned crust on the uplifted surface at large eruption rates (~1 km^3 per year, Richards et al., 1989), which may be accompanied by giant dike swarms (Ernst & Buchan, 2001), layered intrusions, and magmatic underplating (Phillips et al. 1990; Thybo & Artemieva, 2013; Ernst et al., 2019). For a typical mantle viscosity of about 10^{20} Pa s, which is consistent with expected mantle viscosities on Hesperian Mars (Plesa et al., 2018), most uplift takes place over 5 Myr and flood basalt eruption lasts until at least 5 to 10 Myr after the surface reaches its maximum elevation (Griffiths & Campbell, 1991; Friedrich et al. 2018). 4) The plume head dissipates, leading to a phase of thermal subsidence

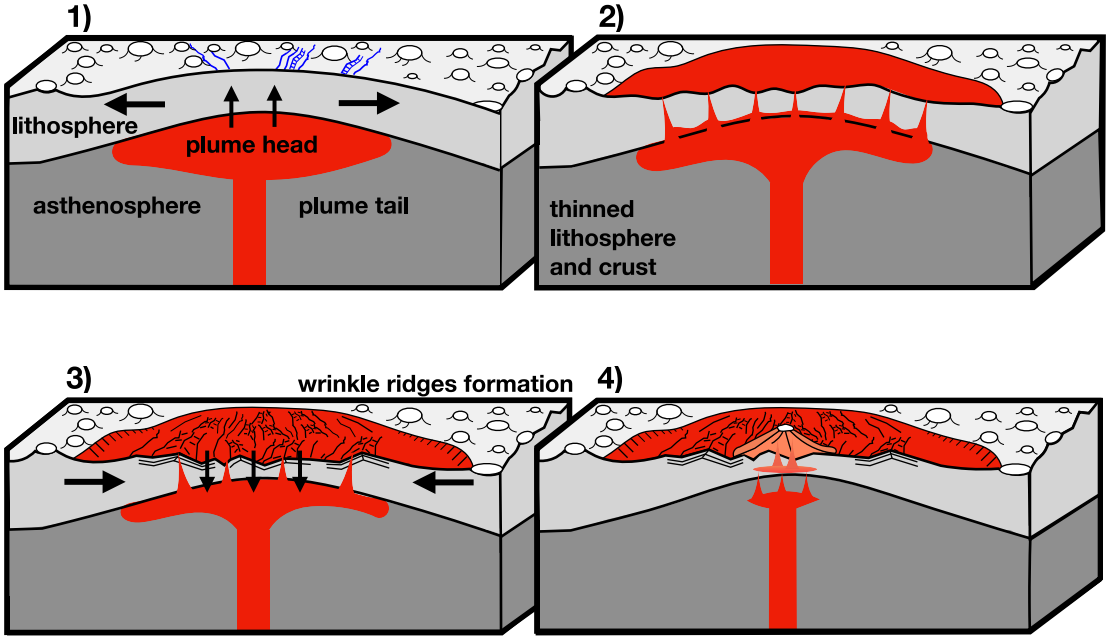

Figure 2 A typical sequence of plume induced flood basalt formation as expected on a one-plate planet, including 1) uplift and extension, 2) flood volcanism, 3) subsidence and compression, and 4) continued volcanism and shield building (see text for details).

and lithospheric thickening. With a lack of thermal support, the province transitions to net downward flexural loading from the prior volcanism and crustal thinning, leading to a state of compression (Campbell, 2001). 5) Flood basalt volcanism ends, but plume tail materials may continue to flow upward from the conduit and may form a volcanic complex and thermally erode the lithosphere (Davies 1994). On the Earth, plume-induced uplift often triggers rifting and continent breakup following stage 3 above, and continued plume-tail activity creates a hotspot chain of volcanic islands in the over-riding plate. In contrast, on a stagnant lid planet, all of the above stages would be recorded in the same geographic region.

The most important aspect of this idealized sequence for this study is that most of the flood basalts form in a stress-free condition on the uplifted surface, followed by later subsidence. Therefore, the uppermost lava flows will not record tensile but compressional strains as the plume-induced uplift subsides down. On Earth, subsidence would coincide with or follow rifting, such that compression is typically not recorded on the flood basalts (Mège & Ernst, 2001). The plume-induced thermal uplift is reversible, and the strains accumulated during uplift will be proportional to the later compressional strains recorded on the flood basalts. Some anelastic effects will also affect the uplift and later subsidence as expressed in the underlying lithosphere (e.g., crustal thinning and tectonic failure, see section 4.3).

3 Hesperia Planum observations

3.1 Topography, gravity, and magnetic field

Hesperia Planum is a 1700-km diameter volcanic plain that sits in a 1 to 1.5 km depression with respect to the surroundings, and that is superimposed by two low-relief volcanic shields, Tyrrhena (106°E -21°N) and Hadriaca (93°E -30°N) Montes (Figure 3A). A geologic investigation by Ivanov et al. (2005) also noted the depression and observed that valley networks generally flow towards the planum and are buried by the ridged plains. That study proposed that the depression was present before the flood lavas erupted, and is thus not associated with the formation

279 of Hesperia Planum. Instead, a sequence of massive magmatically induced erosion
280 of the volatile-saturated regolith was proposed.

281 However, we note that there are a few issues to the scenario proposed in the
282 study of Ivanov et al. (2005). Although valley networks around the periphery do
283 flow toward the planum, it is the ten-kilometer scale roughness of the southern
284 highlands that controls valley orientations, as that creates steeper slopes (~0.5%;
285 Kreslavsky & Head, 1999) than the long-wavelength depression of Hesperia
286 Planum (~0.1%). As such, it is difficult to interpret long-wavelength paleo-
287 topography based on river valley networks in the southern highlands. No
288 reorientation of fluvial valleys is expected for any plume uplift/subsidence
289 sequence. Locally, the edge of the volcanic flows will tend to abut against local
290 topographic highs and embay any valley networks, and this relationship is expected
291 even if Hesperia Planum were uplifted during volcanism. Moreover, erosion of 1
292 km by melting of ground ice would require a regional massive ice deposit of 1 km
293 in thickness, or melting of 10% pore ice down to a depth of 10 km. Deposition of
294 this material within Hellas would then require transport by ~1500 km across a
295 region with no net slope toward the basin. The outflow channels themselves do not
296 show evidence for affecting an area beyond the Hellas rim.

297

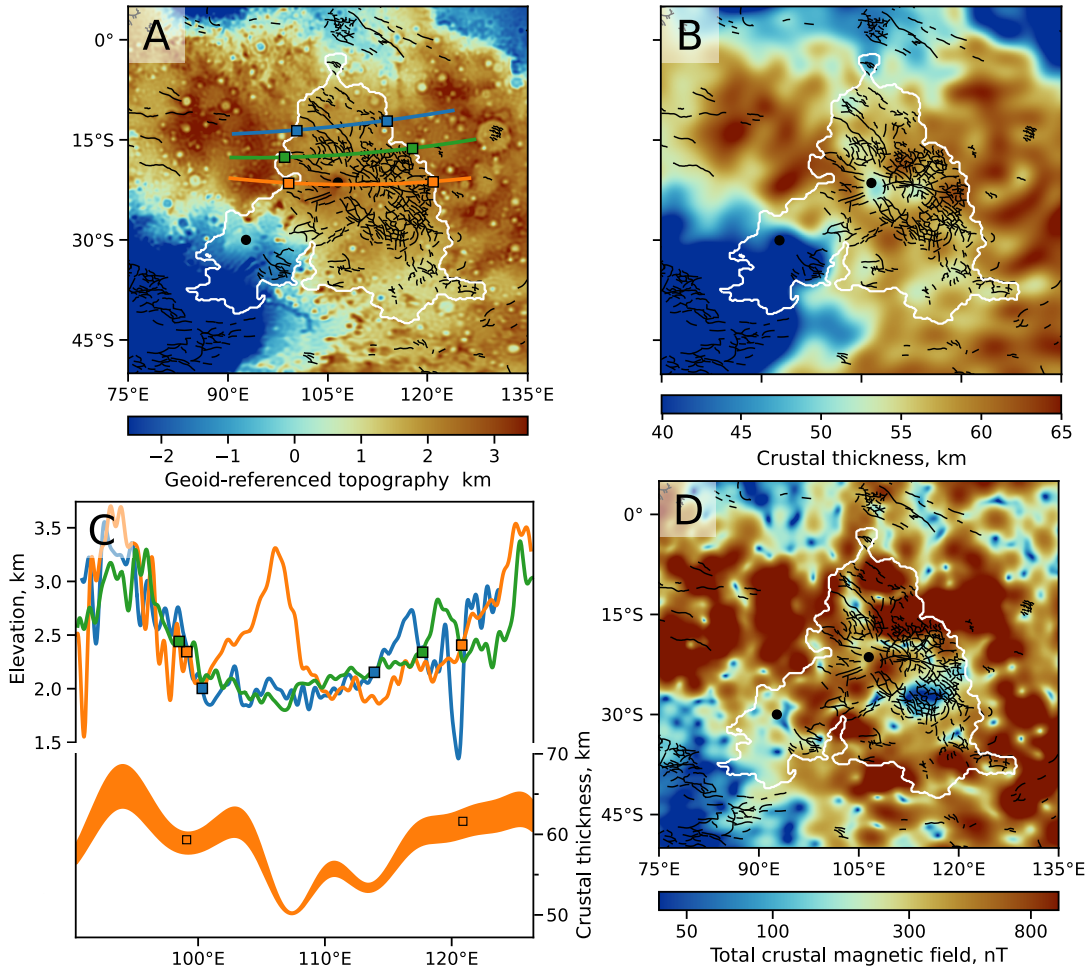

298

299 **Figure 3** Surface elevation, crustal thickness, and magnetic field at Hesperia Planum.
300 (**A**) Surface elevations with color-coded profiles (Smith et al., 2001). (**B**) Representative
301 crustal thickness model assuming a crust density of 2800 kg m^{-3} and mean thickness of
302 50 km. (**C**) Extracted elevation profiles across Hesperia Planum, left axis, and example
303 crustal thickness models for the profile shown in orange, right axis. The crustal
304 thickness models are from Wieczorek et al. (2022) and assume crustal densities of 2700
305 to 2900 kg m^{-3}. (**D**) Total crustal magnetic field with a logarithmic color scale (Langlais
306 et al., 2019). For geologic context, the images are annotated with a white contour of
307 Hesperia Planum, black lines for compressive tectonic features, and black dots for
308 Tyrrhena (106°E -21°N) and Hadriaca (93°E -30°N) Montes. Squares on the profiles
309 denote the edges of the planum. Most of the compressive tectonic features are wrinkle
310 ridges.

The gravity field at Hesperia Planum is also inconsistent with surface erosion to form its low-relief (Figure S1). If the depression were a result of erosion, the planum should be characterized by a long-wavelength gravity low with respect to the surrounding highlands (~120 mGal lower, assuming 1 km of erosion of materials with a density of 2800 kg m^{-3}, see also Evans et al., 2010). Instead, Hesperia Planum's mean gravity field is similar to that of the surrounding highlands both having values of 60±50 mGal (Figure S1). Crustal thickness models that satisfy gravity, topography, and InSight measurements (Wieczorek et al., 2022) further predict a long-wavelength crustal thinning within Hesperia Planum, with a crust that is on average 3 to 5 km thinner than in the surrounding highlands (Figure 3B and C). Alternatively, the gravity signature of the planum could be interpreted as due to a local increase in crustal density (~100 kg m^{-3}) on a flat crust. The loss of pore space associated with the plume-induced heating could have contributed to increasing the local bulk density of the crust. This implies a weak lithospheric support of local bottom loading to compensate for the low-relief, rather than surface erosion. We conclude that it is thus unlikely that the bulk of the planum's depression is due to surface erosion, though some erosion has occurred at the rim of Hellas (Tanaka et al., 2002).

At Hesperia Planum, crustal thinning reaches its maximum value of up to 10 km underneath Tyrrhena Mons (Figure 3B and C), which may be the result of using a crustal density lower than expected locally at Tyrrhena Mons (about 3200 kg m^{-3}, Broquet & Wieczorek 2019), but could also include contributions from a

333 magma chamber below the volcano. A second focused zone of crustal thinning
334 east of Tyrrhena Mons is near the center of a cluster of wrinkle ridges. There is no
335 topography associated with this zone of predicted crustal thinning, and thus the
336 true cause must lie in the subsurface (e.g., a solidified magma chamber, a zone of
337 reduced porosity perhaps associated with high heat flow, or true crustal thinning).
338 We finally note that magmatic underplating of the crust by low-density mantle
339 materials is thought to have occurred in some plume-induced flood basalts on
340 Earth (Thybo & Artemieva, 2013) and also on Mars (Phillips et al., 1990), and this
341 would induce an apparent crustal thickening. Given that this is oppositite to what
342 is observed at Hesperia Planum, underplating is either overcompensated or these
343 materials have been advected back into the mantle and have not lasted to present-
344 day. Volcanism may also leave behind a dense mantle residuum, but this would
345 also likely be advected back into the mantle on short geologic timescales.

346 Within Hesperia Planum, the magnetic field is seen to vary significantly
347 from a minimum of 10 to a maximum of 2500 nT on the ridged plains, with a mean
348 value of 560 nT, and decreases in the vicinity of Hellas (Figure 3D). Interestingly,
349 a ~400 km circular magnetic low (<50 nT), one order of magnitude lower than the
350 planum's mean magnetic field, located where wrinkle ridges cluster (~114°E
351 26°S), stands out from the planum and is also surrounded by a larger circular region
352 of somewhat reduced magnetic field strength (<300 nT). This demagnetized zone
353 is consistent with a scenario in which the crust was heated by local intrusions

354 above the Curie temperature of its magnetic carriers, as is further discussed in
355 section 6.2.

356 3.2 Fault density and strain

357 The tectonic record may provide the most relevant record of the geodynamic
358 evolution of Hesperia Planum. The planum is covered by wrinkle ridges, with high
359 concentrations near 114°E 23°S and 116°E 28°S (Knapmeyer et al., 2006, Figure 4).
360 Over Hesperia Planum, the wrinkle ridge density has a mean value of 0.85×10^{-5} m^{-1},
361 but reaches higher values of 2.73×10^{-5} m^{-1} (Figure 4A), where the density was
362 obtained by dividing the ridge length by the enclosing area and smoothed using a
363 moving average 240 km-diameter Gaussian window. Based on a similar tectonic
364 analysis for the entire Martian surface, we found that Hesperia Planum is characterized
365 by the highest density of wrinkle ridges on the planet.

366 The average tectonic strain over the planum is about 1.91×10^{-3}, reaching a peak
367 value of 4.75×10^{-3} (Figure 4B), where the strain was computed as the wrinkle ridges
368 density multiplied by the ridge height and the cotangent of the fault dip, here assumed
369 to be constant with a value of 30° (see Andrews-Hanna, 2020). For this study, we are
370 primarily interested in the wrinkle ridge cluster described above, and we have thus
371 defined a circular 850-km-diameter area that includes the two peaks, where the mean
372 strain is 3.20×10^{-3} (Figure 4B). For comparison, over Terra Cimmeria's late Noachian
373 units, which are of likely volcanic origin and similar in age to Hesperia Planum at the
374 Noachian-Hesperian boundary (Tanaka et al., 2014), we obtained a mean strain of

375 ~1.76×10^{-3}. This value is slightly higher than our estimated global average for all
376 Hesperian units, ~1.47×10^{-3}. Planetary cooling models predict similar contractional
377 strains to those observed outside of Hesperia Planum, on the order of 2.0×10^{-3} since
378 the Noachian-Hesperian boundary, though they depend on modelling assumptions
379 (e.g., Hauck & Phillips, 2002; Andrews-Hanna et al., 2008). Although this range of
380 strain values is consistent with the mean strain at Hesperia Planum, it is only half of
381 that over the characteristic peak strain area. These values reveal that global contraction
382 is not the only process that generated tectonics on Hesperia Planum.

383

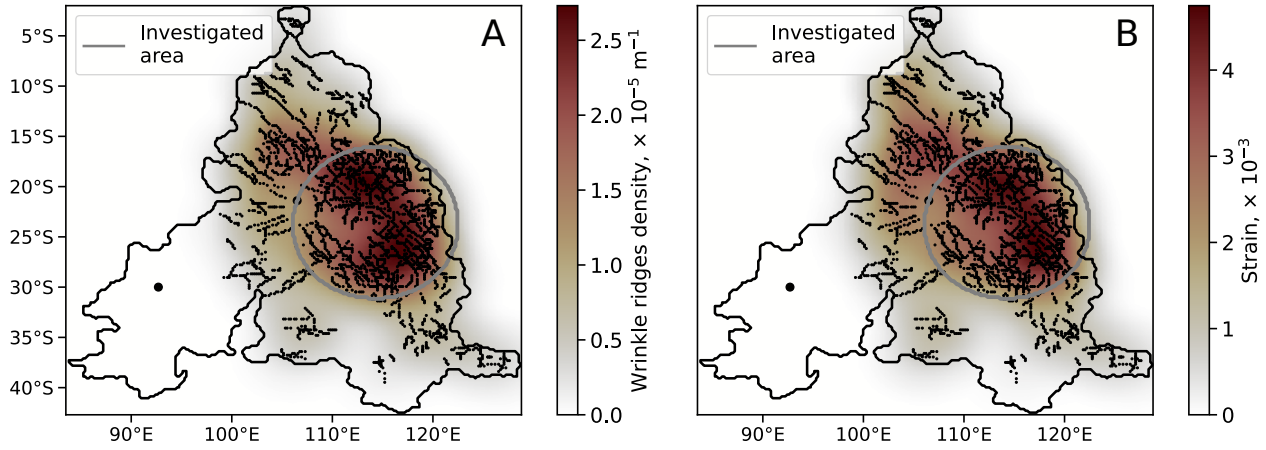

384

385 **Figure 4** The compressional tectonic record at Hesperia Planum based on the mapping
386 of Knapmeyer et al. (2006), showing the calculated wrinkle ridge density (**A**) and strain
387 (**B**). We note that some wrinkle ridges in the vicinity of the Hellas impact basin (near
388 32°S, 98°E) have been ignored. Black dots indicate the location of Tyrrhena (106°E -
389 21°N) and Hadriaca (93°E -30°N) Montes.

390

3.3 Age relationships

Age relationships between the different structures within Hesperia Planum can be useful to unveil relative formation sequences. The highlands surrounding the planum are thought to be early to middle Noachian (4.1–3.8 Ga) in age and among the oldest surfaces on Mars (Tanaka et al., 2014). The ridged plains of Hesperia Planum have ages ranging from about 3.5 to 3.7 Ga (Williams et al., 2010), whereas age estimates for Tyrrhena and Hadriaca Montes vary from ~3.2 and 4.0 Ga (Williams et al., 2008; 2009; Robbins et al., 2011). At face value, and given the overlapping ages, it is unclear whether these volcanoes formed prior to or concomitant with the volcanic plains and could have acted as the major source for their formation.

However, we note that the youngest ages for Tyrrhena Mons (~3.2 Ga) are likely associated with erosion of the pyroclastic deposits on the flanks rather than the formation of the volcano itself. The oldest ages (3.8 or 4.0 Ga, with the younger age for the stratigraphically lower unit; Williams et al., 2008) rely on a very small number of large impact craters and are thus highly uncertain (4 craters with diameter >4 km in each of two units). The older ages of Tyrrhena Mons and Hesperia Planum overlap at the 1-sigma uncertainty level, and thus should be considered indistinguishable (Williams et al., 2008; 2010). The volcanic shields and the ridged plains of Hesperia Planum further have different age biases. Whereas the high standing relief of a volcano will continue to be exposed to cratering and be less susceptible to volcanic resurfacing, the low-lying flood basalts and ridged plains will always be overprinted by younger

412 flows. One important observation, however, is that the caldera of Tyrrhena Mons is
413 younger than the lava plains, with a surface age of 3.4 Ga (Robbins et al., 2011). This
414 reveals that a major episode of Tyrrhena Mons' volcanic activity postdates the
415 formation of the volcanic plains of Hesperia Planum, as would be expected in a plume-
416 induced flood basalt sequence (Figure 2).

417 **4 Methods**

418 In this study, we apply three distinctly different geophysical models to
419 investigate the formation of Hesperia Planum. In the first analysis (section 4.1), we
420 probe the structure of the lithosphere by making simplifying assumptions regarding
421 the nature of surface and subsurface loading, varying the governing parameters in
422 an attempt to fit the spectral ratio of observed gravity and topography data (i.e., the
423 admittance, e.g., Broquet & Wieczorek, 2019). This model evaluates whether the
424 regional gravity and topography are consistent with an erosional sequence to form
425 Hesperia Planum, as suggested in Ivanov et al. (2005), or instead require a
426 combination of top and bottom loading as might arise from plume-induced crustal
427 thinning. In the second analysis (section 4.2), we invert observed gravity and
428 topography data for the loading, displacement and associated strain using an
429 updated version of thin-shell model presented in Banerdt et al. (1986). This
430 inversion compares the observed tectonic record to modeled strains to test whether
431 Hesperia Planum can be explained by crustal loading preserved in the gravity and
432 topography data, as might arise for an origin through passive volcanism, such as in

response to rise of shallow mantle material beneath a zone of already thinned crust. The third analysis (section 4.3) explores a dynamic scenario in which a sequence of plume induced uplift and subsidence is imprinted in the tectonic record (see Figure 2). This model represents a mantle plume loading the base of the lithosphere and deforming the surface, together with subsequent volcanism. The comparison of the modeled strains to the tectonic record is described in section 4.4.

4.1 Modelling the gravitational signature of Hesperia Planum

We model the lithospheric response of Hesperia Planum using a localized admittance technique (see Broquet & Wieczorek, 2019 for a full description of the model). The model makes use of observed topography data to predict the surface load, flexure, and associated gravity field given input lithospheric and crustal parameters. Internal loads, such as from crustal thickness variations, are also modelled using a subsurface to surface load ratio. The resultant theoretical gravity field at Hesperia Planum is extracted using a nominal spherical cap localization window centered at 108°E 18°S, and with a diameter and bandwidth of 24° and 10 degree, respectively, for an optimal concentration factor (>99%, see Wieczorek & Simons, 2005). This window was designed to include the bulk of Hesperia Planum, while avoiding the Hellas and Isidis impact basins that experienced distinctly different evolutionary paths.

Given that we are interested in the long-wavelength signature of the planum, our inversion fits the observed admittance and correlation functions, using an RMS

(root mean square) misfit equation, between spherical harmonic degrees 13 to 34, which are equivalent to wavelengths of about 1500 and 600 km. Degrees 10 to 12 have been ignored as their admittance signal is large and likely aliased by long-wavelength loads on the planet such as Tharsis and the planetary flattening (see also Belleguic et al., 2005). We perform an exhaustive grid search to determine the best-fit elastic thickness T_e, crustal density ρ_c, ratio between the surface and subsurface loads f, and phase relationship between these loads α. The load ratio can have values less than, equal to, or higher than 1, which correspond to a top-load dominated case, an isostatic state (bottom load equal surface load), or a bottom-load dominated case, respectively (Broquet & Wieczorek, 2019). In the case of surface erosion with no post isostatic adjustment, the load ratio is expected to be zero (no bottom load). Constant parameters include the mantle density, Young's modulus, and Poisson's ratio, which were set to values of 3500 kg m^{-3}, 100 GPa, and 0.25, respectively, following previous admittance studies (Belleguic et al., 2005; Broquet & Wieczorek, 2019).

4.2 Inverting for loading, displacement, and strain from gravity and topography

Whereas the previous section presented a forward model of the gravity field, we here test whether Hesperia Planum, and its characteristic strain record, could have formed from passive volcanism using an inverse approach (Text S2). In this scenario, the geodynamic history of Hesperia Planum, including all loads (mantle or crustal) and associated deformation, is assumed to be fully recorded in the present-day

gravity and topography (unlike the mantle plume model; see below). We invert observed gravity and topography data for the loading, displacement and associated strain using an updated version of thin-shell model presented in Banerdt et al. (1986), which is described in Text S2. This model is similar to classical crust-mantle relief inversions from gravity and topography (e.g., Wieczorek et al., 2022), with the addition that it partitions the crustal thickness variations into top and bottom loads and constrains lithospheric displacement as a function of elastic thickness (Banerdt et al., 1986; Broquet, 2022). The inferred displacement allows us to constrain crustal strains and the direction of faulting, which are compared to the tectonic record. For this model, we assume that there are no internal density variations, which is a common assumption in gravity field inversions (e.g., Wieczorek et al., 2022).

4.3 Modelling a plume induced flood basalt

In a third approach, we explore a dynamic scenario in which flood volcanism at Hesperia Planum originated from a mantle plume source. This scenario assumes that strain during the initial uplift is not imprinted in the tectonic record as it is buried beneath the lava flows (Figure 2). The gravity and topography during uplift are also not preserved, as they would mostly return to their original values after dissipation of the thermal anomaly. However, the compressional strain during subsidence would be recorded in form of wrinkle ridges on the surface of volcanic units, with this strain simply being opposite in sign and equal in orientation and magnitude to the strain during uplift. Any thermal or volcanic erosion of the crust would contribute

496 to additional subsidence beyond that from the cooling of the lithosphere after
497 dissipation of the plume head. Intrusive magmatism would also induce loading, but
498 this will not be accounted for here, as intrusive loading would directly tradeoff with
499 lava flow loading, and both have unknown thicknesses. Thermal erosion and lateral
500 redistribution of magma away from the plume center would enhance the subsidence
501 of the volcanic plains, as observed in some terrestrial large igneous provinces
502 (Campbell et al., 2001; Ernst et al. 2014). Some magmatically-induced surface
503 erosion could explain the heavily degraded state of the rim of Hellas to the south-
504 west of Hesperia Planum (Tanaka et al., 2002; Ivanov et al., 2005). Thus, the strain
505 predicted by elastic subsidence following cooling of the plume head and overlying
506 lithosphere places a lower bound on the actual subsidence.

507 This loading model also uses the thin-shell formalism developed in Banerdt et
508 al. (1986; see text S2), modified to work in a forward sense with unknown gravity
509 and topography, but with a known mantle plume head load. The modeled
510 displacement and strains will also be compared to the tectonic record. To represent
511 a plume-induced uplift of the surface, we assume that the plume head load is
512 compensated by dynamic topography only (i.e., no crustal thickness variation),
513 where upward flexure equals upward surface topography. The plume head is
514 modeled as a density contrast, located underneath the elastic lithosphere, and is
515 tapered by a Tukey-like (a cosine tapered step function) window to a given radius.
516 Based on a series of lab experiments simulating mantle plumes (e.g., Griffiths and
517 Campbell 1991; Campbell, 2007), we assume a flattened plume head diameter with

size of 0.5 to 1 times that of the flood basalt province and an aspect ratio in the range of 0.05 to 0.25, yielding a plume head radius of 425 to 850 km and thickness of 85 to 425 km. Estimates on the thermal anomaly associated with terrestrial mantle plume heads range from 100 to 600 K (e.g., White & McKenzie, 1995), equivalent to a density contrast of about 10 to 70 kg m^{-3}, assuming a thermal expansivity of $3.3\times10^{-5}\,K^{-1}$ (Fei, 1995; Plesa et al., 2018). Following these studies, our inversions explore a wide range of plume head and lithosphere parameters as shown below.

Our dynamic plume model does not account for lithosphere thickness variations during the plume-induced flood basalt sequence. To test the influence of this simplification, we compared the modeled instantaneous flexure at a fixed lithosphere thickness of 80 km to an iterative model with incremental cooling and lithosphere thickening in parallel with the subsidence. The incremental model starts with an initial 350 K plume thermal anomaly underneath a 50-km-thick elastic lithosphere. The thermal anomaly is dissipated linearly, and the elastic thickness is increased accordingly (up to 80 km). The difference between our instantaneous flexure on the 80 km-thickened lithosphere and the incremental model was found to be less than 5% (incremental flexure is slightly higher). However, comparing the instantaneous flexure on the 50 km-thick initial lithosphere and the incremental model gave rise to differences larger than 80% (instantaneous flexure on the thin lithosphere is largely higher). This is simply the result of lithospheric rigidity increasing with the elastic thickness cubed. This result suggests that the best-fit modeled lithosphere thickness will be representative of the thickened elastic

lithosphere at the end of subsidence (or, similarly, the pre-plume background value), rather than the thermally thinned lithosphere during uplift.

Finally, in this theoretical framework, the flood basalt that erupts on the uplifted surface acts as a load and generates additional flexure and compressive strains. Loading, displacement, and strain can be assumed to be linear (Beuthe, 2008), and we thus run a separate model to estimate the deformation contribution coming from the flood lavas. Because there is no topographic signal of central flexure within Hesperia Planum's depression, this independent model assumes that the flexure has been filled by lava flows. We constructed an iterative model where the initial lava thickness is constant everywhere and incrementally increased by flexure until the final surface is flat, as observed today. This model uses as input the initial lava flow thickness, and it is assumed that crustal thickness and internal density variations are negligible. As an example, for an elastic thickness of 100 km, an initial 500 m of lava flows at this scale gives rise to a maximum central flexure of about 1250 m for a maximum final lava thickness of 1750 m. As the thickness of the plains is not well constrained, the initial thickness is varied from 0 to 1 km, along with the elastic thickness of the lithosphere.

4.4 Strain comparison of models to observations

Three independent outputs of our passive (section 4.2) and dynamic (4.3) loading models will be compared to the observed tectonic record. The strain magnitude is compared to observations using the RMS misfit over the restricted

561 area shown in Figure 4, which includes the two characteristic peak strain
562 concentrations. In a second comparison, the observed and predicted strains are
563 normalized relative to their peak values and compared using the RMS misfit over
564 all of Hesperia Planum. Given that some of the observed wrinkle ridges are in
565 locally orthogonal networks (Figure 4), our models compute the areal strain, which
566 is obtained by adding the sum of principal horizontal strains and their product.

567 In a third comparison, the principal directions of faulting are compared using
568 the RMS misfit over the whole Hesperia Planum region. Given that wrinkle ridges
569 are generally linear, the fault strike is calculated as the azimuth between the two-
570 end points and the midpoint mapped by Knapmeyer et al. (2006). The predicted
571 principal direction of faulting is obtained by computing the principal strain
572 direction from the modeled horizontal strains. Given the orthogonal tectonic
573 network, both horizontal stresses are expected to be compressional and ridges of
574 either orientation can be in agreement with the model results. Thus, our misfit to
575 the orientation of faulting is measured relative to the closest of the two principal
576 strain directions, with a maximum value of 45°.

577 Separating these three quantities allows us to focus on specific parameters.
578 For example, the strain magnitude is controlled by the load, which depends on the
579 observed gravity and topography, or the plume head and lava flow thickness, and
580 the density contrast of the plume head. On the other hand, both the normalized
581 strain concentration and direction of faulting will be mostly affected by the elastic
582 thickness of the lithosphere and plume head radius. Finally, we have seen in the

583 previous section that the peak strain recorded in Hesperia Planum is not located at
584 its center. For that reason, we performed an exhaustive grid search where we
585 systematically varied the position of the plume head for the dynamic model (section
586 4.3) along with the plume and lithosphere parameters.

587
588 **5 Results**

589 5.1 The lithospheric properties of Hesperia Planum

590 We first consider results of the admittance and correlation analysis of the top
591 and bottom loading models, which tests whether the gravity and topography at
592 Hesperia Planum are consistent with an erosional sequence (Figure 5). The best-fit
593 model has load ratio of about 1 and is thus nearly isostatic, though values as low as
594 0.1 and up to 7 are acceptable. This result indicates that the depression containing
595 Hesperia Planum is dominantly a result of bottom loading (crustal thinning or
596 density increase) rather than erosion as suggested in Ivanov et al. (2005). Formation
597 of the planum's depression by erosion alone would indicate a load ratio of 0 (no
598 bottom load), which corresponds to a sharp peak in the misfit and can be excluded.
599 The elastic thickness is found to be at least 16 km, with a best-fit of about 62 km.
600 The elastic thickness is potentially thicker than locally at Tyrrhena Mons (10±10
601 km, see Broquet & Wieczorek, 2019), which suggests that the volcano may have
602 formed on a locally thinned lithosphere relative to the thicker lithosphere
603 supporting Hesperia Planum itself. The phase relationship between the surface and
604 bottom load is 0.8 (+0.2, -0.8) and the crustal density is entirely unconstrained, but

the partial decorrelation and lack of crustal density constraints are both expected given the smooth nature of the local topography.

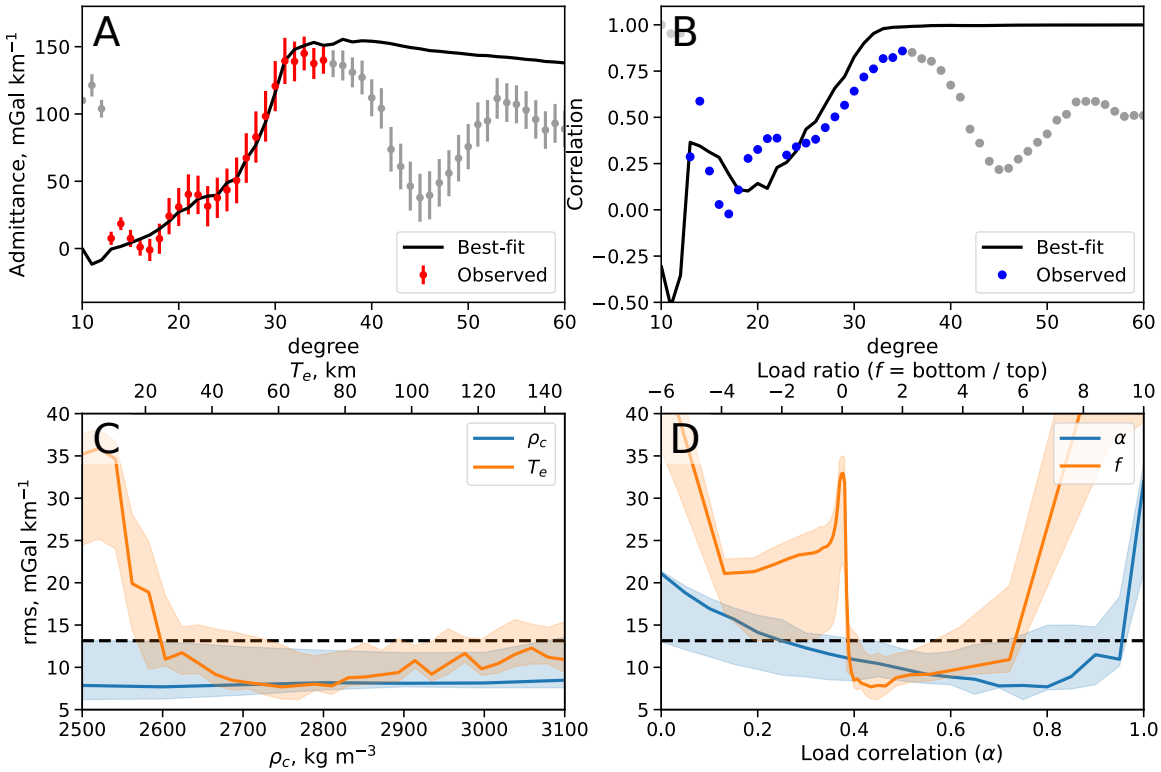

Figure 5 Localized admittance and correlation analysis. Fitted observed (**A**) admittance and associated uncertainty (red) and (**B**) correlation (blue) with our best-fitting models (black). Data points outside the degree range fit by the model are shaded gray in both plots. (**C**) Minimum RMS misfit as a function of crustal density (ρ_c, bottom axis) and elastic thickness (T_e, top axis). (**D**) Minimum RMS misfit as a function of the phase relationship between the surface and bottom load (α, bottom axis) and load ratio (f, top axis). Solid lines give the misfit as a function of one parameter (x-axis) along the minimum misfit for all parameters. The horizontal dashed line in the lower plots indicates the mean uncertainty in the observed admittance from degree 13 to 34. The shaded contour gives the minimum RMS misfit corresponding to variations of the window size (±2°), position (±4° in latitude and longitude), and mean crustal thickness of the model (±10 km).

622 5.2 Displacement, and strain from gravity and topography

623 We next examine the predictions of our passive scenario, in which all loading
624 that has affected Hesperia Planum is reflected in the present-day gravity and
625 topography (excluding the possibility of a past mantle plume). These inversions
626 predict crustal thickness, displacement, and strain, and we note that our crustal
627 thickness models are consistent with Wieczorek et al. (2022). The predicted
628 displacement and strains are dominated by Tyrrhena and Amphitrites Montes
629 (Figure 6), with peak strains of about 1.5 and 6×10^{-3} for elastic thicknesses of 150
630 and 50 km, respectively. These loading strains are significantly higher than
631 observed at these locations in the tectonic record ($\sim1\times10^{-3}$, Figure 4), which
632 suggest that the two shield volcanoes likely formed over long timespan where
633 flexure operated in parallel to volcanic loading. For an elastic thickness of 50 km
634 (Figure 6A and B), the weak extensional and compressional strains predicted at the
635 observed local cluster of wrinkle ridges in eastern Hesperia Planum are
636 inconsistent with the strong compressional strain observed there. For the larger 150
637 km elastic thickness (C and D), most of the planum is in compression, but the
638 magnitude of the predicted strain ($\sim0.45\times10^{-3}$) is 10 times lower than observed in
639 the tectonic record at the local strain concentration ($\sim4.75\times10^{-3}$), and this
640 difference cannot be explained by global contraction alone.

641

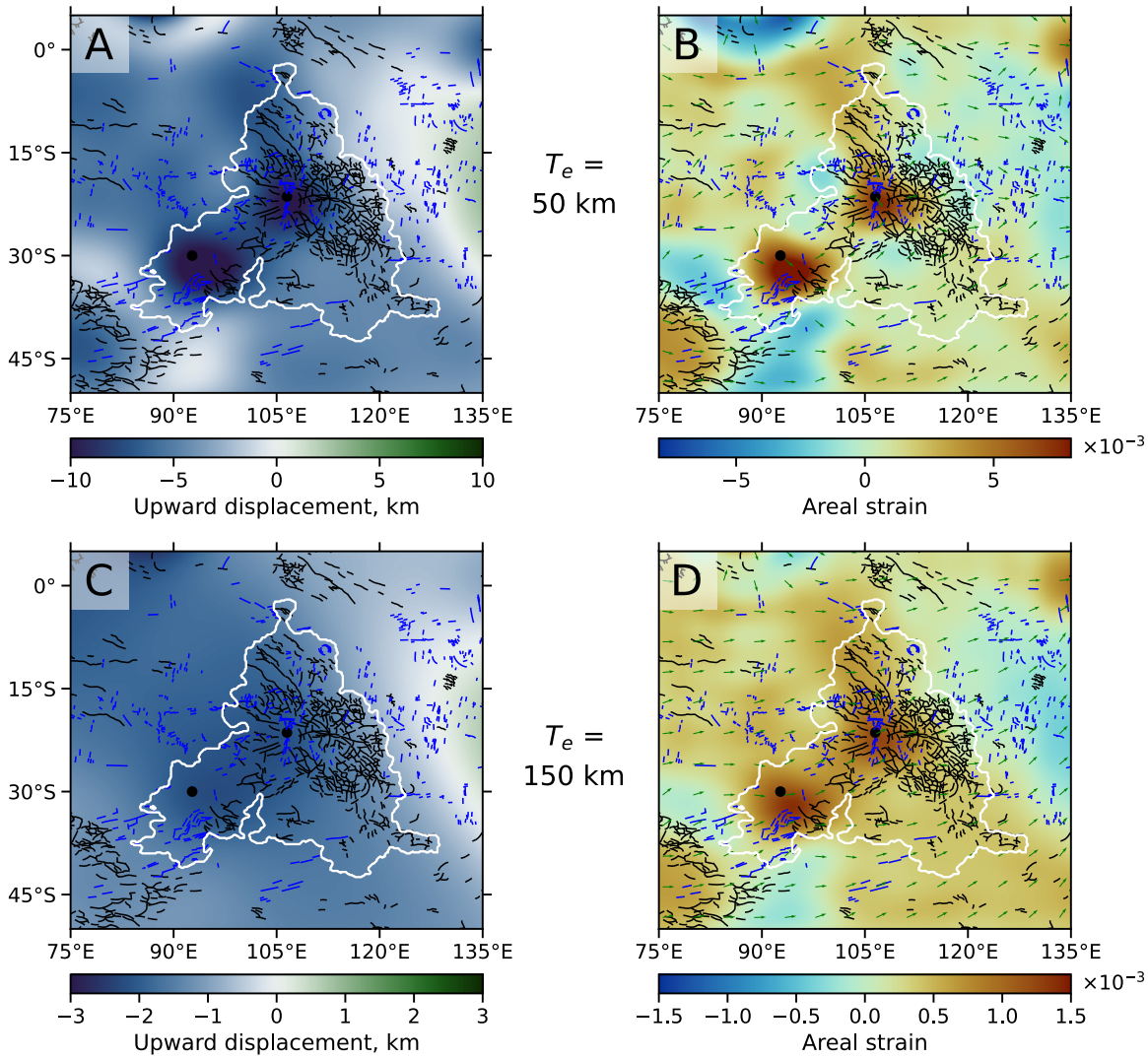

642

643 **Figure 6** Displacement and strain at Hesperian Planum based on a global inversion of
644 gravity and topography for two elastic thicknesses, 50 km (**A, B**) and 150 km (**C, D**).
645 (left) Displacement of the lithosphere, where negative displacements correspond to
646 downward flexure. (right) Predicted areal strain magnitude (color) and principal strain
647 orientation (green arrows), where positive strains correspond to compression. Black
648 dots indicate the location of Tyrrhena (106°E -21°N) and Hadriaca (93°E -30°N)
649 Montes.

650

651 In addition to not fitting the observed strain magnitude, the inferred strain

652 concentration is significantly different from that observed and this model cannot

explain the local strain concentration around 114°E 23°S, nor the inferred strain direction. The RMS difference between the observed normalized tectonic strain concentration and that predicted using elastic thicknesses of 50 and 150 km are about 0.29 and 0.31, respectively, and thus neither model provides a better match to the distribution of strain (these values are primarily useful for comparing models to one another; see below). The RMS difference between the observed azimuth of faulting and that modeled is 27.5°and 29.0° for elastic thicknesses of 50 and 150 km, respectively. For reference, if the wrinkle ridges were randomly arranged, the RMS difference would be about 26°, and thus the predicted azimuth of faulting in these models is incompatible with the observations. Together, these results suggest that the driving mechanism that generated significant compression on Hesperia Planum is not recorded in present-day gravity and topography.

5.3 Predictions of the mantle plume model

Finally, we consider the predictions of the dynamic model in which a sequence of plume uplift and subsidence is responsible for the observed tectonic strain. We first limit ourselves to the case of plume effects alone, not accounting for an additional contribution from the flood basalt loading. The fit to the plume head radius and location is based only on the tectonic strain concentration and fault orientations (Figure 7), and the other plume head and lithosphere parameters were obtained from fitting the strain magnitude within the peak strain area at Hesperia Planum after correcting for the subsequent global contraction (Figure S2).

674 To determine the plume head center position, we compared the predicted strain
675 concentration and azimuth of faulting to the tectonic record for various input
676 parameters and plume locations. The minimum misfit between the tectonic and
677 modeled strain concentration is obtained when the plume is centered where wrinkle
678 ridges cluster, near 114°E 22°S for plume head radii of 600 to 800 km (Figure 7, left).
679 Placing the plume center within ±2° latitude and ±4° longitude of that location provides
680 better fits to the strain concentration than did the global gravity and topography in the
681 previous section, with RMS misfits of 0.17–0.22 versus 0.29. The misfit between the
682 predicted azimuth of faulting and observed pattern of wrinkle ridges is also minimized
683 for a plume centered near 114°E 22°S (Figure 7, right), and better fits the data for the
684 plume model than our previous inversions, with a minimum value of 22.5° versus
685 27.5°. Additional low misfit solutions are found for plume heads centered close to the
686 edge of the planum to the north-west, south-east, and south-west. These plume center
687 locations are allowed because of the orthogonal pattern of wrinkle ridges, but are
688 inconsistent with the strain concentration. Thus, the fits to those two independent
689 quantities suggest a similar plume location around 114±4°E 22±2°S, which is about
690 400 km east of Tyrrhena Mons. These tectonic analyses further show that Tyrrhena
691 Mons is not the preferred plume head center, with higher misfits of ~0.30 and 27°, as
692 a few ridges appear circumferential and radial about Tyrrhena Mons, but the majority
693 show no clear relationship to the central volcano. Nevertheless, we acknowledge that
694 some ridges could have formed following the evolutionary sequence and loading of

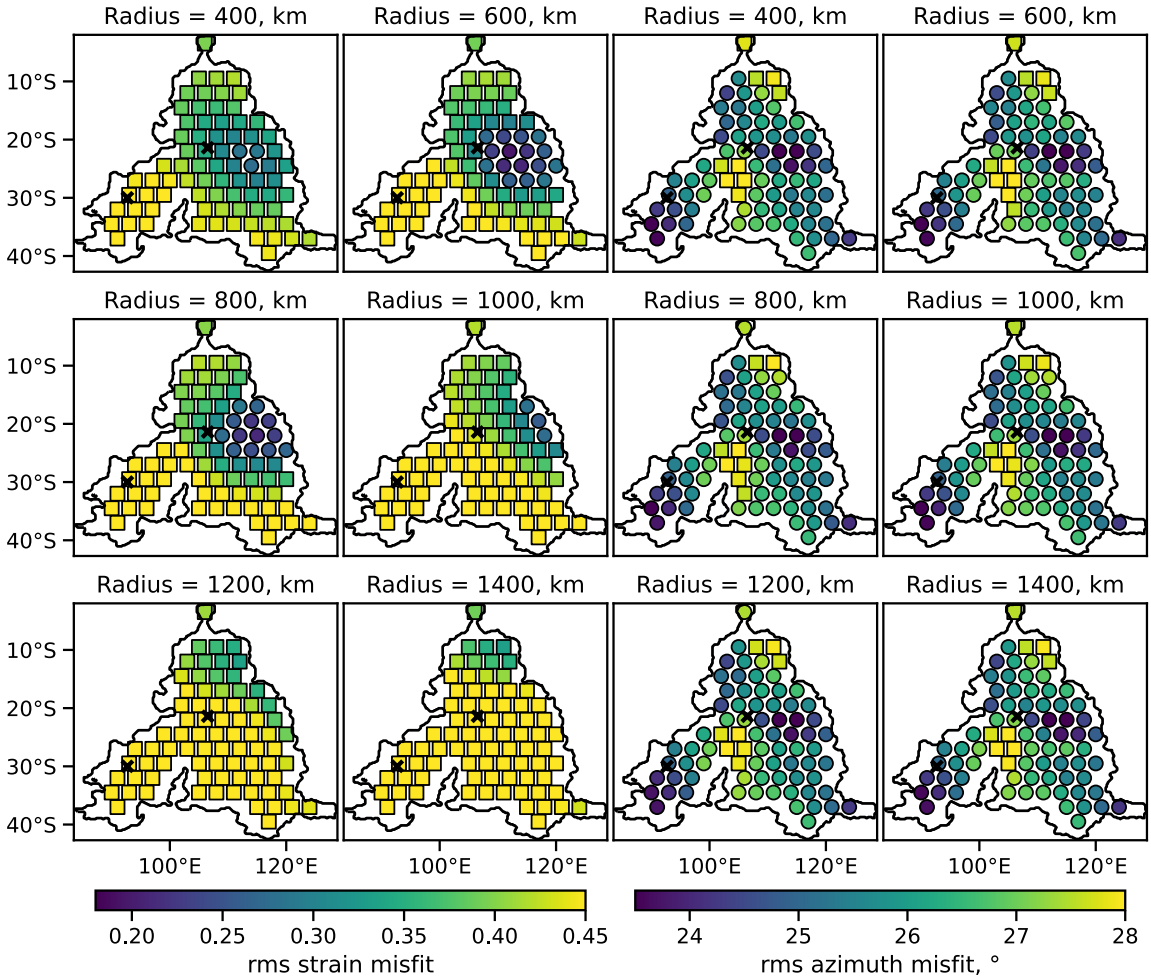

Figure 7 Plume head center at Hesperia Planum. Influence of the plume head radius on the RMS misfit between the observed and modeled strain concentration (2 leftmost columns) and azimuth (2 rightmost columns) as a function of the position the plume head (colored markers). The elastic thickness, plume head density and aspect ratio were set to 120 km, -35 kg m^{-3}, and 0.20 respectively. Where the RMS misfit is lower than from the global gravity and topography inversion (27.5°) location markers are dots, and are squares elsewhere. The black crosses indicate the position of Tyrrhena and Hadriaca Montes.

that shield volcano, as it is predicted to be associated with large compressive strains (Figure 6).

Using this same approach, we find similar best-fit plume locations for all parameters we investigated (Figure S3, S4, and S5), and we suggest that the paleo-plume center was located near 114±4˚E 22±2˚S. Large elastic thicknesses (>75 km)

700 better reproduce the observed strain concentration (Figure S3), but varying the density
701 contrast and aspect ratio of the plume head was found to not significantly influence the
702 predicted strain pattern (Figure S4 and S5). This is to be expected given that these two
703 parameters have a minor influence on the wavelength of deformation, which controls
704 the strain concentration and azimuth.

705 Next, we make use of the best-fit plume location and determine what parameters
706 best reproduce the observed strain magnitude (Figure S2, Text S3). For the models
707 with no flood lavas, the plume head density contrast should be at least -25 kg m^{-3}
708 (thermal anomaly of about 215 K) for an aspect ratio of less than 0.25, and up to -40
709 kg m^{-3} (~350 K) assuming an aspect ratio of 0.15. The minimum aspect ratio is
710 obtained for the largest density contrast investigated (-60 kg m^{-3}) and is 0.11, and any
711 elastic thickness can satisfy the data (Figure S2). For these parameters our predicted
712 uplifts range from 1 to 5 km. Importantly, though subject to large tradeoffs (Text S3),
713 these ranges of accepted parameters are consistent with plume head characteristics as
714 constrained on Earth (section 4.3), and imply that the observed tectonic record can be
715 explained solely by the dynamics of an Earth-like mantle plume. When accounting for
716 the presence of the flood basalt, with an initial thickness of 500 m, less strain is
717 required to originate from the plume head. The density contrast and aspect ratio are
718 both reduced, with minimum allowed values down to -10 kg m^{-3} and 0.09, respectively
719 (Figure S2).

720 In summary, the best-fit model has a plume head centered at 114°E 22°S, with
721 a radius of 700 km and thickness of 280 km. The best-fit plume head density contrast

722 is -35 kg m^{-3} (Figure 8A) and is located underneath a 120-km thick elastic
723 lithosphere. This model predicts about 2.8 km of plume-induced uplift (B), which is
724 consistent with the terrestrial record (e.g., Sengör, 2001; Saunders et al., 2007). Post-
725 subsidence compressional strain is predicted to concentrate where wrinkle ridges
726 cluster (Figure 8C), and thus better explains the distribution of strain than the passive
727 volcanic loading scenario (Figure 6). Comparing the normalized modeled and
728 observed strain distributions gives an RMS misfit of 0.17, which is significantly
729 lower than found with passive volcanic loading only (0.29). In the restricted
730 investigated area, the mean strain value is about 1.61×10^{-3}, which compares
731 favorably to the observed value of $1.44–1.73\times10^{-3}$, where we have corrected the
732 latter for a global contractional strain of $1.47–1.76\times10^{-3}$ (section 3.2). The predicted
733 azimuth of faulting (Figure 8D) provides a better fit to the observed orthogonal and
734 short-wavelength strain pattern, with an RMS misfit of 22.5°, which is better than
735 for both a random distribution (26°) and the predictions from the passive model
736 (27.5°). That there is still a substantial mismatch in wrinkle ridge orientations

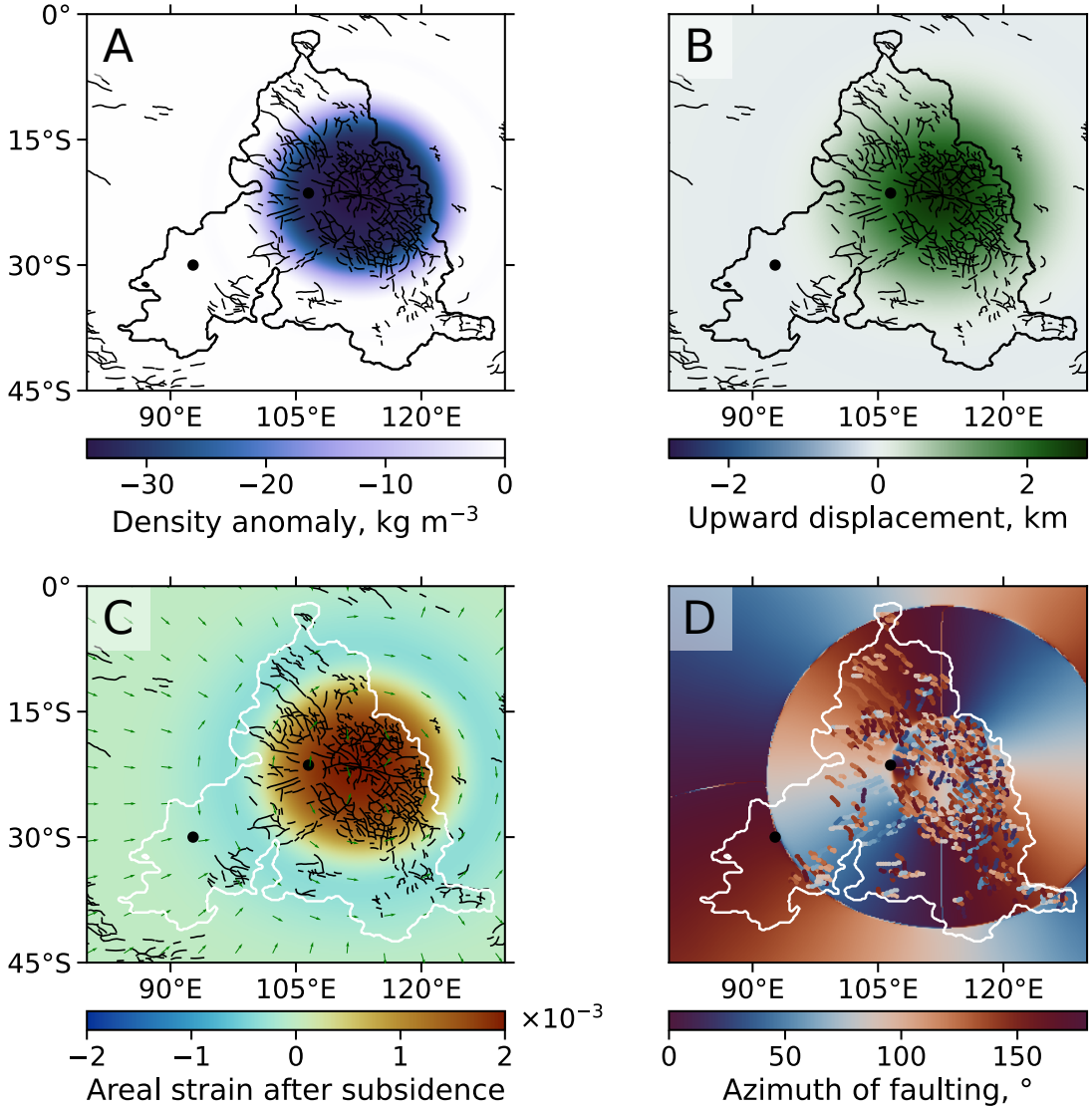

Figure 8 Best-fitting example of displacement and strain for a plume located at 114°E 22°S assuming a plume aspect ratio of 0.2 and an elastic thickness of 120 km. (**A**) The assumed density anomaly for a plume head radius of 700 km and density contrast of -35 kg m^{-3}, (**B**) the vertical displacement, (**C**) the areal strain magnitude after subsidence of the uplift (color) and maximum strain direction (green arrows), and (**D**) the predicted azimuth of faulting (background map) in comparison to observed wrinkle ridges (superposed lines).

737 indicates that other factors may also be influencing fault orientations, including pre-

738 existing basement structures and other sources of non-isotropic strain. We note that

over much of the plume area, the difference between the two horizontal compressional strain magnitudes is small, and the orientation of faulting is not strongly controlled by these stresses.

6 Discussion – Implications of a mantle plume origin

6.1 Position of the mantle plume and relative formation sequence of Hesperia Planum

In its simplest sense, a plume model for the origin of Hesperia Planum would predict a transition from plume-induced uplift and flood basalt eruption to shield building, all focused on the plume center (Figure 2). In order to fit the observed tectonic record, we have constrained the plume head to have been located near 114°E 22°S when most of the deformation occurred. This position correlates with a cluster of wrinkle ridges and local crustal thinning (Figure 3B and C), but is about 400 km east of Tyrrhena Mons. Age relationships based on crater counting suggest that the ages of Tyrrhena Mons and Hesperia Planum overlap, with a major phase of shield volcanism postdating the lava plain formation (section 3.3). If the plume model is correct, it must be reconciled with the evolution of volcanism in both space and time.

Given the lack of plate tectonics on Mars, the offset between the plume center, the center of Hesperia Planum, the magnetic anomaly (see section 6.2), and Tyrrhena Mons may be explained by asymmetric plume flattening or plume drift driven by mantle flow patterns. Both have been observed in the terrestrial record (Camp, 1995; Jordan et al.,

2004, Tarduno et al., 2003; Konrad et al., 2018), and are predicted to occur in geodynamic models (e.g., Steinberger, 2000; Arnould et al., 2019). The simplest explanation for the temporal evolution would be that the bulk of Tyrrhena Mons is younger than the bulk of Hesperia Planum, in which case the volcanic shield formed from plume tail material after the main flood basalt sequence. Given uncertainties in the ages of both features, this scenario is consistent with observations.

6.2 Demagnetization and elastic thickness

Further insights into the elastic thickness and thermal anomaly associated with the plume head can be obtained by investigating the crustal magnetic field. The circular 400-km-diameter magnetic low, centered at 114°E 26°S, is located close to where wrinkle ridges cluster, within our expected plume head radius and only about 240 km away from the best-fit center. Based on its shape and position, it is possible that this magnetic low reflects the initial impingement of the hot mantle plume that partly thermally demagnetized the lithosphere before flattening and cooling underneath it. Laboratory experiments have constrained the flattened plume head to be generally about 3 times the initial spherical plume diameter (e.g., Griffiths & Campbell, 1991), and this would be consistent with our model favoring a final plume diameter of 1200 to 1600 km (3 to 4 times the size of the demagnetized region). Areas with decreased magnetism have also been shown to correlate with the presence of magmatic underplating, representing the paleo-plume location, in some terrestrial large igneous provinces (Blanchard et al., 2017; Ernst et al., 2019).

In order for the crust to be thermally demagnetized, most of the crust bearing the magnetic carrier should be raised above the Curie temperature, which is about 850–950 K considering hematite and magnetite as the most likely magnetic minerals of the crust (e.g., Dunlop & Arkani-Hamed, 2005). To first order, the 850–950 K isotherm is about the temperature at the base of the elastic lithosphere for a standard wet rheology (e.g., Plesa et al., 2018). This implies that the depth of magnetization is representative of the thickness of the elastic lithosphere. A localized power spectrum analysis found the depth of magnetization to be highest in the Hesperia Planum, at 50 to 90 km (Gong & Wieczorek, 2021). Given that the Curie temperature isotherm (roughly equal to the elastic thickness) must be deeper than the bounds on the depth of magnetization, the results of Gong and Wieczorek imply that the elastic thickness of the lithosphere is larger than 50 to 90 km, which is consistent with our preferred elastic thicknesses that are greater than 75 km (section 5.3). Similarly, the local demagnetization near the center of our preferred plume location indicates that the Curie isotherm and base of the lithosphere at this location were shallower at one point during the evolution of the planum, consistent with the thermal effects of a mantle plume.

7 Conclusions

The late Noachian to early Hesperian volcanic ridged plains represent a major episode in the geodynamic evolution of Mars, but little is known about the context of their formation. Flood basalts at Hesperia Planum have the highest density of

802 wrinkle ridges on the planet, suggesting a unique magmatic-tectonic evolution.
803 Together with the planum's characteristic tectonic record, its local surface
804 depression, bottom loading (crustal thinning or density increase), and
805 magnetization reveal that Hesperia Planum was subject to a significant geologic
806 event that heated and deformed the lithosphere. Our tectonic analysis has shown
807 that the planum displays a clear local concentration of wrinkle ridges with a
808 compressional strain of 3.20×10^{-3} on average and up to 4.75×10^{-3}. Both are
809 significantly higher than on similarly aged surfaces (~$1.47–1.76\times10^{-3}$) or than
810 predicted by thermal evolution models (~2.0×10^{-3}, Hauck & Phillips, 2001;
811 Andrews-Hanna et al. 2008). Using a flexural loading model based on present-day
812 gravity and topography, we have demonstrated that the observed depression is not
813 a result of an erosional event, and that the observed compression cannot be the
814 result of passive volcanic loading.

815 We have explored the possibility that Hesperia Planum formed dynamically,
816 as plume-induced flood basalts following an evolutionary path similar to that of
817 some continental flood basalts on Earth (e.g., Richards et al., 1989; Campbell &
818 Griffiths, 1990; Campbell, 2007). In this scenario, the surface would have recorded
819 significant strains during a reversible sequence of uplift and subsidence, while the
820 present-day gravity and topography would not preserve a record of this loading.
821 The plume-induced uplift model is able to explain the observed peak strain
822 magnitude, strain concentration, and wrinkle ridge orientations. The best-fit plume
823 and lithosphere parameters are consistent with both terrestrial observations (White

824 & McKenzie, 1989; Saunders et al., 2007) and the seminal laboratory experiments
825 by Griffiths & Campbell (1990). Based on the fit to the tectonic record, the best-fit
826 paleo-plume head center was located around 114°E 22°S. The presence of a plume
827 at that location correlates with and provides a robust explanation for the presence
828 of a local circular magnetic low, where we favor a partial crustal demagnetization
829 associated with the initial spherical plume head before it flattened underneath the
830 lithosphere.

831 This study has used Hesperia Planum as an archetype for a larger class of
832 similar Noachian-Hesperian highland volcanic provinces, which includes Malea
833 Planum and Syrtis Major. These provinces formed during discrete geodynamic
834 episodes that were distinct from the contemporaneous volcanism that was largely
835 focused in the Tharsis region (Carr & Head, 2010). Our results suggest that the
836 Noachian-Hesperian martian mantle was not only characterized by a giant degree-
837 1 upwelling beneath Tharsis, but also by several smaller localized mantle plumes
838 with Earth-like characteristics. Our analysis of the formation sequence for Hesperia
839 Planum and its similarity to the evolution of large igneous provinces on Earth
840 supports the hypothesis that some highland volcanic provinces on Mars may
841 formed as a result of large plumes arising from the deep mantle.

842

Acknowledgments

The thin-shell flexural model can be found at Broquet (2022), and the main equations are given in Text S2. The spherical harmonic model of the gravity field is available at Zuber et al. (2010), and the color maps used in this study are from Crameri (2018). Some of this work made use of the SHTOOLS package of Wieczorek & Meschede (2018). A.B. kindly thanks the Laboratoire Lagrange of the Observatoire de la Côte d'Azur for hosting him during portions of this work, and A. Lasbordes for fruitful discussion. We thank Richard Ernst and an anonymous reviewer for their comments that helped improve the manuscript. This work was supported by grant 80NSSC17K0059 from the NASA Solar System Workings program to JCAH.

References

Anderson, D. L. (2000). The thermal state of the upper mantle; no role for mantle plumes. *Geophysical Research Letters, 27*(22), 3623–3626. https://doi.org/10.1029/2000GL011533.

Andrews-Hanna, J. C. (2020). The tectonic architecture of wrinkle ridges on Mars. *Icarus, 351*, 113937. https://doi.org/10.1016/j.icarus.2020.113937.

Andrews-Hanna, J. C., Zuber, M. T., & Hauck II, S. A. (2008). Strike-slip faults on Mars: Observations and implications for global tectonics and geodynamics. *Journal of Geophysical Research: Planets, 113*(E8). https://doi.org/10.1029/2007JE002980.

Arnould, M., Ganne, J., Coltice, N., & Feng, X. (2019). Northward drift of the azores plume in the Earth's mantle. *Nature Communication 10*(3235). https://doi.org/10.1038/s41467-019-11127-7.

Banerdt, W. B. (1986). Support of long-wavelength loads on Venus and implications for internal structure. *Journal of Geophysical Research: Solid Earth 91*, 403–419. https://doi.org/10.1029/JB091iB01p00403.

Banerdt, W. B., Phillips, R. J., Sleep, N. H., & Saunders, R. S. (1982). Thick shell tectonics on one-plate planets: Applications to Mars. *Journal of Geophysical Research: Solid Earth, 87*(B12), 9723–9733. https://doi.org/10.1029/JB087iB12p09723.

Belleguic, V., Logonné, P., & Wieczorek, M. A. (2005). Constraints on the Martian lithosphere from gravity and topography data. *Journal of Geophysical Research: Planets, 110*(E11005). https://doi.org/10.1029/2005JE002437.

Bethell, E. M., Ernst, R. E., & Samson, C. (2022). Analysis of Venusian wrinkle ridge morphometry using stereo-derived topography: A case study from Southern Eistla Regio. *Journal of Geophysical Research: Planets, 127*, e2021JE006879, https://doi.org/10.1029/2021JE006879.

Beuthe, M. (2008). Thin elastic shells with variable thickness for lithospheric flexure of one-plate planets. *Geophysical Journal International, 172*(2), 817–841. https://doi.org/10.1111/j.1365-246X.2007.03671.x.

885 Blanchard, J. A., Ernst, R. E., & Samson, C. (2017). Gravity and magnetic
886 modelling of layered mafic–ultramafic intrusions in large igneous
887 province plume centre regions: case studies from the 1.27 Ga
888 Mackenzie, 1.38 Ga Kunene–Kibaran, 0.06 Ga Deccan, and 0.13–0.08
889 Ga High Arctic events. *Canadian Journal of Earth Sciences*, *54*(3),
890 290–310. https://doi.org/10.1139/cjes-2016-0132.
891 Buchan, K. L., & Ernst, R. E. (2021). Plumbing systems of large igneous
892 provinces (LIPs) on Earth and Venus: Investigating the role of giant
893 circumferential and radiating dyke swarms, coronae and novae, and
894 mid-crustal intrusive complexes, *Gondwana Research*, *100*, 25–43.
895 https://doi.org/10.1016/j.gr.2021.02.014
896 Broquet, A. (2022). AB-Ares/Displacement strain planet: Version 0.4.0.
897 *Zenodo*. https://doi.org/10.5281/zenodo.5784417.
898 Broquet, A., & Wieczorek, M. A. (2019). The gravitational signature of
899 Martian volcanoes. *Journal of Geophysical Research: Planets, 124*(8),
900 2054–2086. https://doi.org/10 .1029/2019JE005959.
901 Camp, V. E. (1995). Mid-Miocene propagation of the Yellowstone mantle
902 plume head beneath the Columbia River basalt source region. *Geology,*
903 *23*(5), 435–438. https://doi.org/10.1130/0091-
904 7613(1995)023h0435:MMPOTYi2.3.CO;2.
905 Camp, V. E. (2013). Origin of Columbia River Basalt: Passive rise of
906 shallow mantle, or active upwelling of a deep-mantle plume? In *The*

Columbia River Flood Basalt Province. Geological Society of America. https://doi.org/10.1130/2013.2497(07).

Campbell, I. H. (2007). Testing the plume theory. *Chemical Geology, 241*(3), 153–176. https://doi.org/10.1016/j.chemgeo.2007.01.024.

Campbell, I. H., & Griffiths, R. W. (1990). Implications of mantle plume structure for the evolution of flood basalts. *Earth and Planetary Science Letters, 99*(1), 79–93. https://doi.org/10.1016/0012-821X(90)90072-6.

Campbell, I. H. (2001). Identification of ancient mantle plumes. *In:* Ernst R. E., & Buchan, K. L. (eds.) Mantle Plumes: Their Identification Through Time. *Special Papers-Geological Society of America, 352*, 5–22. https://doi.org/10.1130/0-8137-2352-3.5

Carr M. H., & Head J. W. (2010). Geologic history of Mars, *Earth and Planetary Science Letters 294*, 185–203 (2010). https://doi.org/10.1016/j.epsl.2009.06.042.

Coffin, M. F., and Eldholm, O. (1994), Large igneous provinces: Crustal structure, dimensions, and external consequences, *Rev. Geophys.*, *32*(1), 1– 36, https://doi.org/10.1029/93RG02508.

Courtillot, V., Jaupart, C., Manighetti, I., Tapponnier, P., & Besse, J. (1999). On causal links between flood basalts and continental breakup. *Earth and Planetary Science Letters, 166*(3), 177–195. https://doi.org/10.1016/S0012-821X(98)00282-9.

928 Crameri, F. (2018). Scientific colour maps: perceptually uniform and colour-
929 vision deficiency friendly. *Zenodo*.
930 https://doi.org/10.5281/zenodo.1243862.
931 Davies, G. F. (1994), Thermomechanical erosion of the lithosphere by mantle
932 plumes, *Journal of Geophysical Research, 99*(B8), 15709–15722,
933 https://doi.org/10.1029/94JB00119.
934 Davies, G. F. (2000). *Dynamic Earth: Plates, plumes and mantle convection*.
935 Cambridge University Press.
936 Dunlop, D. J., & Arkani-Hamed, J. (2005), Magnetic minerals in the Martian
937 crust, *Journal of Geophysical Research, 110*, E12S04,
938 https://doi.org/10.1029/2005JE002404.
939 Ernst, R. E., & Buchan, K. L. (2001). The use of mafic dike swarms in
940 identifying and locating mantle plumes. In *Mantle plumes: their*
941 *identification through time.* Geological Society of America.
942 https://doi.org/10.1130/0-8137-2352-3.247.
943 Ernst, R. E., Grosfils, E. B., & Mège, D. (2001). Giant Dike Swarms: Earth,
944 Venus, and Mars. *Annual Review of Earth and Planetary*
945 *Sciences, 29*(1), 489–534.
946 https://doi.org/10.1146/annurev.earth.29.1.489.
947 Ernst, R. E., & Desnoyers, D.W (2004). Lessons from Venus for
948 understanding mantle plumes on Earth. *Physics of the Earth and*

Planetary Interiors, 146, 195–229.
https://doi.org/10.1016/j.pepi.2003.10.012.

Ernst, R. E. (2014). Introduction, definition, and general characteristics. Large Igneous Province (eds R. E. Ernst). *Cambridge University Press,* 1–39. https://doi.org/10.1017/CBO9781139025300.001.

Ernst, R. E., Liikane, D. A., Jowitt, S. M., Buchan, K. L., Blanchard, J. A. (2019). A new plumbing system framework for mantle plume-related continental large igneous provinces and their mafic-ultramafic intrusions. *Journal of Volcanology and Geothermal Research*, *384*, 75–84. https://doi.org/10.1016/j.jvolgeores.2019.07.007.

Ernst, R. E., Bond, D. P. G., Zhang, S.-H., Buchan, K. L., Grasby, S. E., Youbi, N., El Bilali, H., Bekker, A., & Doucet, L. S. (2021). Large Igneous Province Record Through Time and Implications for Secular Environmental Changes and Geological Time-Scale Boundaries. In Large Igneous Provinces (eds R. E. Ernst, A. J. Dickson and A. Bekker). https://doi.org/10.1002/9781119507444.ch1

Evans, A. J., Andrews-Hanna, J. C., & Zuber, M. T. (2010). Geophysical limitations on the erosion history within Arabia Terra, *J. Geophys. Res.*, *115*, E05007. https://doi.org/10.1029/2009JE003469.

Farnetani, C. G., & Richards, M. A. (1994). Numerical investigations of the mantle plume initiation model for flood basalt events. *Journal of*

970 *Geophysical Research: Solid Earth, 99*(B7), 13813–13833.
971 https://doi.org/10.1029/94JB00649.
972 Fei, Y. (1995). Thermal expansion. In *Mineral physics & crystallography*
973 (pp. 29–44). American Geophysical Union (AGU).
974 https://doi.org/10.1029/RF002p0029.
975 Foulger, G. (2010). *Plates vs. plumes: A geological controversy*. Wiley-
976 Blackwell. https://doi.org/10.1002/9781444324860.
977 Friedrich A. M., Bunge H.-P., Rieger S. M., Colli L., Ghelichkhan S., &
978 Nerlich R. (2018). Stratigraphic framework for the plume mode of
979 mantle convection and the analysis of interregional unconformities on
980 geological maps. *Gondwana Research, 53,* 159–188.
981 https://doi.org/10.1016/j.gr.2017.06.003.
982 Geikie, A. (1880). The lava-fields of north-western Europe. *Nature, 23*, 3–5.
983 https://doi.org/10 .1038/023003a0.
984 Genova, A., Goossens, S., Lemoine, F. G., Mazarico, E., Neumann, G. A.,
985 Smith, D. E., & Zuber, M. T. (2016). Seasonal and static gravity field of
986 Mars from MGS, Mars Odyssey and MRO radio science. *Icarus, 272*,
987 228–245. https://doi.org/10.1016/j.Icarus.2016.02.050.
988 Golombek, M. P., & Phillips, R. J.(2009). Mars tectonics. In T. R. Watters &
989 R. A. Schultz (Eds.), *Planetary tectonics* (pp. 183–232). Cambridge
990 University Press. https://doi.org/10.1017/CBO9780511691645.006.

991 Gong, S., & Wieczorek, M. (2021). Depth of Martian magnetization from
992 localized power spectrum analysis. *Journal of Geophysical Research:*
993 *Planets, 126, e2020JE006690*. https://doi.org/10.1029/2020JE006690.
994 Greeley, R., & Schneid, B. D. (1991). Magma generation on Mars: Amounts,
995 rates, and comparisons with Earth, Moon, and Venus. *Science*,
996 *254*(5034), 996–998. https://doi.org/10.1126/science.254.5034.996.
997 Griffiths, R. W., & Campbell, I. H. (1990). Stirring and structure in mantle
998 starting plumes. *Earth and Planetary Science Letters, 99*(1), 66–78.
999 https://doi.org/10.1016/0012-821X(90)90071-5.
1000 Griffiths, R. W., & Campbell, I. H. (1991). Interaction of mantle plume heads
1001 with the Earth's surface and onset of small-scale convection. *Journal of*
1002 *Geophysical Research: Solid Earth, 96*(B11), 18295–18310.
1003 https://doi.org/10.1029/91JB01897.
1004 Gülcher, A. J. P., Gerya, T. V., Montési, L. G. J., & Munch J. (2020). Corona
1005 structures driven by plume–lithosphere interactions and evidence for
1006 ongoing plume activity on Venus. *Nat. Geosci., 13*, 547–554.
1007 https://doi.org/10.1038/s41561-020-0606-1
1008 Hales, T. C., Abt, D. L., Humphreys, E. D., & Roering, J. J. (2005). A
1009 lithospheric instability origin for Columbia river flood basalts and
1010 Wallowa mountains uplift in northeast Oregon. *Nature, 438*, 842–845.
1011 https://doi.org/10.1038/nature04313.

1012 Hansen, V. L. (2007). LIPs on Venus. *Chemical Geology, 241*, 354–374.
1013 https://doi.org/10.1016/j.chemgeo.2007.01.020.
1014 Hauck, S. A., & Phillips R. J. (2002). Thermal and crustal evolution of Mars.
1015 *Journal of Geophysical Research, 107*(E7).
1016 https://doi.org/10.1029/2001JE001801.
1017 Head, J. W., & Coffin, M. (1997). Large igneous provinces: A planetary
1018 perspective. In *Large igneous provinces: Continental, oceanic, and*
1019 *planetary flood volcanism* (pp. 411–438). American Geophysical Union
1020 (AGU). https://doi.org/10.1029/ GM100p0411.
1021 Head, J. W., Kreslavsky, M. A., & Pratt, S., (2002). Northern lowlands of
1022 Mars: Evidence for widespread volcanic flooding and tectonic
1023 deformation in the Hesperian Period, *J. Geophys. Res.*, *107*(E1),
1024 https://doi.org/10.1029/2000JE001445.
1025 Head, J. W., Wilson, L., Dickson, J., & Neukum, G. (2006). The Huygens-
1026 Hellas giant dike system on Mars: Implications for late Noachian–early
1027 Hesperian volcanic resurfacing and climatic evolution. *Geology, 4*(34),
1028 285–288. https://doi.org/10.1130/G22163.1.
1029 Hooper, P. R., Camp, V. E., Reidel, S. P., & Ross, M. E. (2007). The origin
1030 of the Columbia River flood basalt province: Plume versus non plume
1031 models. In *Plates, Plumes and Planetary Processes.* Geological
1032 Society of America. https://doi.org/10.1130/2007.2430(30).

1033 Hooper, P. R., & Conrey, R. M. (1989). A model for the tectonic setting of
1034 the Columbia River basalt eruptions. In *Volcanism and Tectonism in the*
1035 *Columbia River Flood-Basalt Province.* Geological Society of America.
1036 https://doi.org/10.1130/SPE239-p293.
1037 Ivanov, M. A., Korteniemi, J., Kostama, V.-P., Aittola, M., Raitala, J.,
1038 Glamoclija, M., Marinangeli, L., & Neukum, G. (2005). Major episodes
1039 of the hydrologic history in the region of Hesperia Planum, Mars.
1040 *Journal of Geophysical Research: Planets, 110*(E12).
1041 https://doi.org/10.1029/2005JE002420.
1042 Jordan, B. T., Grunder, A. L., Duncan, R. A., & Deino, A. L. (2004).
1043 Geochronology of age-progressive volcanism of the Oregon high lava
1044 plains: Implications for the plume interpretation of Yellowstone.
1045 *Journal of Geophysical Research: Solid Earth, 109*(B10).
1046 https://doi.org/10.1029/2003JB002776.
1047 Knapmeyer, M., Oberst, J., Hauber, E., Wählisch, M., Deuchler, C., &
1048 Wagner, R. (2006). Working models for spatial distribution and level of
1049 Mars' seismicity. *Journal of Geophysical Research: Planets, 111*(E11).
1050 https://doi.org/10.1029/2006JE002708.
1051 Konrad, K. D., Koppers, A. A. P., Steinberger, B., Finlayson, V. A., Konter,
1052 J. G., & Jackson, M. G. (2018). On the relative motions of long-lived
1053 Pacific mantle plumes. *Nature Communication, 9*(854).
1054 https://doi.org/10.1038/s41467-018-03277-x.

1055 Korteniemi, J., Raitala, J., Aittola, M., Ivanov, M. A., Kostama, V.-P.,
1056 Teemu, O., & Hiesinger, H. (2010). Dike indicators in the Hadriaca
1057 Patera–Promethei Terra region, Mars. *Earth and Planetary Science*
1058 *Letters, 294*(3), 466–478. https://doi.org/10.1016/j.epsl.2009.06.038.
1059 Kreslavsky, M. A., & Head, J. W. (1999). Kilometer-scale slopes on Mars
1060 and their correlation with geologic units: Initial results from Mars
1061 Orbiter Laser Altimeter (MOLA) data. *Journal of Geophysical*
1062 *Research: Planets, 104*(E9), 21911–21924.
1063 https://doi.org/10.1029/1999JE001051.
1064 Langlais, B., Thébault, E., Houliez, A., Purucker, M. E., & Lillis, R. J.
1065 (2019). A new model of the crustal magnetic field of Mars using MGS
1066 and MAVEN. *Journal of Geophysical Research: Planets*, *124*(6), 1542–
1067 1569. https://doi.org/10.1029/ 2018JE005854.
1068 Laske, G., Masters., G., Ma, Z. & Pasyanos, M., Update on CRUST1.0 - A 1-
1069 degree Global Model of Earth's Crust, *Geophys. Res. Abstracts, 15,*
1070 *Abstract* EGU2013-2658, 2013.
1071 MacLellan, L., Ernst, R., El Bilali, H., Ghail, R., & Bethell, E. (2021).
1072 Volcanic history of the Derceto large igneous province, Astkhik
1073 Planum, Venus. *Earth-Science Reviews, 220.*
1074 https://doi.org/10.1016/j.earscirev.2021.103619.
1075 Montési, L. G. J., & Zuber, M. T. (2003). Clues to the lithospheric structure
1076 of Mars from wrinkle ridge sets and localization instability. *Journal of*

Geophysical Research: Planets, 108(E6). https://doi.org/10.1029/2002JE001974.

Morgan, W. (1971). Convection plumes in the lower mantle. *Nature, 230*, 42–43. https://doi.org/10.1038/230042a0.

Mège, D., & Ernst, R. E. (2001). Contractional effects of mantle plumes on Earth, Mars, and Venus. In *Mantle plumes: their identification through time.* Geological Society of America. https://doi.org/10.1130/0-8137-2352-3.103.

Phillips, R. J., Sleep, N. H., & Banerdt, W. B. (1990). Permanent Uplift in Magmatic Systems With Application to the Tharsis Region of Mars. *Journal of Geophysical Rese*arch 95, 5089– 5100. https://doi.org/10.1029/jb095ib04p05089.

Petersen, K.D., Schiffer, C. & Nagel, T (2018). LIP formation and protracted lower mantle upwelling induced by rifting and delamination. *Sci Rep* 8, 16578. https://doi.org/10.1038/s41598-018-34194-0

Plesa, A.-C., Padovan, S., Tosi, N., Breuer, D., Grott, M., Wieczorek, M. A., Spohn, T., Smrekar, S. E., & Banerdt, W. B. (2018). The thermal state and interior structure of Mars. *Geophysical Research Letters, 45*(22), 12,198–12,209. https://doi.org/10.1029/2018GL080728.

Rainbird, R., Ernst, R. E. (2001). The sedimentary record of mantle-plume uplift, *In:* Ernst R. E., Buchan, K. L. (eds.) Mantle Plumes: Their

1098 Identification Through Time. *Geological Society of America Special*
1099 *Paper, 352*, 227–245. https://doi.org/10.1130/0-8137-2352-3.227.
1100 Redmond, H. L., & King, S. D. (2004). A numerical study of a mantle plume
1101 beneath the Tharsis Rise: Reconciling dynamic uplift and lithospheric
1102 support models. *Journal of Geophysical Research* 109, E09008.
1103 https://doi.org/10.1029/2003JE002228. Reidel, S. P., Camp, V. E.,
1104 Tolan, T. L., Kauffman, J. D., & Garwood, D. L. (2013). Tectonic
1105 evolution of the Columbia River flood basalt province. In *The*
1106 *Columbia River Flood Basalt Province.* Geological Society of America.
1107 https://doi.org/10.1130/2013.2497(12).
1108 Reidel, S. P., Fecht, K. R., Hagood, M. C., & Tolan, T. L. (1989). The
1109 geologic evolution of the central Columbia Plateau. In *Volcanism and*
1110 *Tectonism in the Columbia River Flood-Basalt Province.* Geological
1111 Society of America. https://doi.org/10 .1130/SPE239-p247.
1112 Richards, M. A., Duncan, R. A., & Courtillot, V. E. (1989). Flood basalts and
1113 hotspot tracks: Plume heads and tails. *Science, 246*(4926), 103–107.
1114 https://doi.org/10.1126/ science.246.4926.103.
1115 Robbins, S. J., Achille, G. D., & Hynek, B. M. (2011). The volcanic history
1116 of Mars: High-resolution crater-based studies of the calderas of 20
1117 volcanoes. *Icarus, 211*(2), 1179–1203.
1118 https://doi.org/10.1016/j.icarus.2010.11.012.

1119 Saunders, A. D., Jones, S. M., Morgan, L. A., Pierce, K. L., Widdowson, M.,
1120 & Xu, Y. G. (2007). Regional uplift associated with continental large
1121 igneous provinces: The roles of mantle plumes and the lithosphere.
1122 Chemical Geology, 241(3), 282–318.
1123 https://doi.org/10.1016/j.chemgeo.2007.01.017.
1124 Schultz, R. A. (2000), Localization of bedding plane slip and backthrust
1125 faults above blind thrust faults: Keys to wrinkle ridge structure, *J.*
1126 *Geophys. Res.*, 105(E5), 12035– 12052, doi:10.1029/1999JE001212.
1127 Scott, D. H., & Tanaka, K. L. (1986). Geologic map of the western equatorial
1128 region of Mars: U.S. geological survey misc. inv. map i-1802-a.
1129 https://doi.org/10.3133/i1802A.
1130 Sengör, A. M. C. (2001). Elevation as indicator of mantle-plume activity. In
1131 *Mantle plumes: their identification through time.* Geological Society of
1132 America. https://doi.org/10.1130/0-8137-2352-3.183.
1133 Smith, D. E., Zuber, M. T., Frey, H. V., Garvin, J. B., Head, J. W.,
1134 Muhleman, D. O., Pettengill, G. H., Phillips, R. J., Solomon, S. C.,
1135 Zwally, H. J., Banerdt, W. B., Duxbury, T. C., Golombek, M. P.,
1136 Lemoine, F. G., Neumann, G. A., Rowlands, D. D., Aharonson, O.,
1137 Ford, P. G., Ivanov, A. B., Johnson, C. L., McGovern, P. J., Abshire, J.
1138 B., Afzal, R. S., & Sun, X. (2001). Mars Orbiter Laser Altimeter:
1139 Experiment summary after the first year of global mapping of Mars.

Journal of Geophysical Research: Planets, 106(E10), 23689–23722. https://doi.org/10.1029/2000JE001364.

Solomon, S. C. (1978). On volcanism and thermal tectonics on one-plate planets. *Geophysical Research Letters, 5*(6), 461–464. https://doi.org/10.1029/GL005i006p00461.

Steinberger, B. (2000). Plumes in a convecting mantle: Models and observations for individual hotspots. *Journal of Geophysical Research: Solid Earth, 105*(B5), 11127–11152. https://doi.org/10.1029/1999JB900398.

Tanaka, K. L., Kargel, J. S., MacKinnon, D. J., Hare, T. M., & Hoffman, N. (2002). Catastrophic erosion of Hellas basin rim on Mars induced by magmatic intrusion into volatile-rich rocks. *Geophysical Research Letters, 29*(8), 37-1–37-4. https://doi.org/10.1029/2001GL013885.

Tanaka, K. L., Skinner, J. A. Jr., Dohm, J. M., Irwin, R. P. III, Kolb, E. J., Fortezzo C. M., Platz, T., Michael, G. G., & Hare, T. M. (2014). Geologic map of Mars: U.S. geological survey scientific investigations map 3292, scale 1:20,000,000. *pamphlet*, 43. https://doi.org/10.3133/sim3292.

Tarduno, J. A., Duncan, R. A., Scholl, D. W., Cottrell, R. D., Steinberger, B., Thordarson, T., Kerr, B. C., Neal, C. R., Frey, F. A., Torii, M., & Carvallo, C. (2003). The emperor seamounts: Southward motion of the

Hawaiian hotspot plume in Earth's mantle. *Science, 301*(5636), 1064–1069. https://doi.org/10.1126/science.1086442.

Thybo, H., & Artemieva, I. M. (2013). Moho and magmatic underplating in continental lithosphere. *Tectonophysics, 609,* 605–619. https://doi.org/10.1016/j.tecto.2013.05.032.Torsvik, T. H., Burke, K., Steinberger, B., Webb, S. J., & Ashwal, L. D. (2010). Diamonds sampled by plumes from the core–mantle boundary. *Nature, 466*, 352–355. https://doi.org/10.1038/nature09216.

Watters, T. R. (1989). Periodically spaced anticlines of the Columbia Plateau. In *Volcanism and Tectonism in the Columbia River Flood-Basalt Province.* Geological Society of America. https://doi.org/10.1130/SPE239-p283.

White, R. S., & McKenzie, D. (1989). Magmatism at rift zones: The generation of volcanic continental margins and flood basalts. *Journal of Geophysical Research: Solid Earth, 94*(B6), 7685–7729. https://doi.org/10.1029/JB094iB06p07685.

White, R. S., & McKenzie, D. (1995). Mantle plumes and flood basalts. *Journal of Geophysical Research: Solid Earth, 100*(B9), 17543–17585. https://doi.org/10.1029/ 95JB01585.

Wieczorek, M. A., & Meschede, M. (2018). Shtools: Tools for working with spherical harmonics. *Geochemistry, Geophysics, Geosystems, 19*, 2574–2592. https://doi.org/10.1029/2018GC007529.

1183 Wieczorek, M. A., & Simons, F. J. (2005). Localized spectral analysis on the
1184 sphere. *Geophysical Journal International, 162*, 655–675.
1185 https://doi.org/10.1111/ j.1365-246X.2005.02687.x.
1186 Wieczorek, M. A., Broquet, A., McLennan, S. M., Rivoldini, A., Golombek,
1187 M., Antonangeli, D., et al. (2022). InSight constraints on the global
1188 character of the Martian crust. *Journal of Geophysical Research:*
1189 *Planets, 127*, e2022JE007298. https://doi.org/10.1029/2022JE007298.
1190 Williams, D. A., Greeley, R., Werner, S. C., Michael, G., Crown, D.
1191 A., Neukum, G., and Raitala, J. (2008), Tyrrhena Patera: Geologic
1192 history derived from *Mars Express* High Resolution Stereo Camera, *J.*
1193 *Geophys. Res.*, 113, E11005, https://doi.org/10.1029/2008JE003104.
1194 Williams, D. A., Greeley, R., Fergason, R. L., Kuzmin, R., McCord, T. B.,
1195 Combe, J.-P., Head, J. W., Xiao, L., Manfredi, L., Poulet, F., Pinet, P.,
1196 Baratoux, D., Plaut, J. J., Raitala, J., Neukum, G. (2009). The Circum-
1197 Hellas Volcanic Province, Mars: Overview. *Planetary and Space*
1198 *Science, 57*, 895–916. https://doi.org/10.1016/j.pss.2008.08.010.
1199 Williams, D. A., Greeley, R., Manfredi, L., Raitala, J., & Neukum, G. (2010).
1200 The Circum-Hellas volcanic province, Mars: Assessment of wrinkle-
1201 ridged plains. *Earth and Planetary Science Letters, 294*(3), 492–505.
1202 https://doi.org/10.1016/j.epsl.2009.10.007.

1203 Wilson, L., & Head, J. W. (1983). A comparison of volcanic eruption
1204 processes on Earth, Moon, Mars, Io and Venus. *Nature, 302*, 663-–669.
1205 https://doi.org/10.1038/ 302663a0.
1206 Wilson, T. J. (1965). Evidence from ocean islands suggesting movement in
1207 the Earth. *Philosophical Transactions of the Royal Society of London.*
1208 *Series A, Mathematical and Physical Sciences, 258*.
1209 https://doi.org/10.1098/rsta.1965.0029.
1210 Zuber, M. T., Konopliv, A., & Lemoine, F. G. (2010). *MRO radio science*
1211 *derived gravity science data products v1.0*. NASA Planetary Data
1212 System. https://doi.org/10.17189/1519521

Supplementary Materials for

Plume-Induced Flood Basalts on Hesperian Mars: An Investigation of Hesperia Planum

A. Broquet*, J. C. Andrews-Hanna

Correspondence to: adrienbroquet@email.arizona.edu

This PDF file includes:

Supplementary Text

S1. Plume head size.

Several parameters influence the diameter of a plume head in the mantle (D), including the rise height through the mantle (Z), the kinematic viscosity (v), and the gravitational attraction (g), which all are expected to differ between the Earth and Mars, where (Campbell & Griffiths, 1990; Griffiths & Campbell 1991) $D \sim Z^{3/5}(v/g)^{1/5}$.

On Earth, plume heads are predicted to have diameters ranging from 1000–1200 km in the mantle (with a viscosity of 10^{20} Pa s), and flatten at the base of the lithosphere to reach diameters of 2000–2400 km (Griffiths & Campbell, 1991; White & McKenzie, 1995). On Mars, constraints on the Hesperian mantle viscosity are scarce and we assume a large range of viscosities from $10^{19–21}$ Pa s (Plesa et al., 2018). For a plume coming from the core-mantle boundary, plume heads would have diameters of 530 to 1600 km in the mantle, and 1060 to 3200 km after flattening. Our model results with a flattened plume head diameter of 1400 km are thus consistent with expected plume head sizes on Mars.

S2. An updated thin-shell model for displacement and strain calculations.

The thin-shell formalism used in this study is based on the initial formulation of Banerdt (1986) and can be found at Broquet (2022). Various improvements have been made to the initial formulation to include finite-amplitude correction and filtering (Wieczorek & Phillips, 1998), but also lateral density variations at any arbitrary depth (Wieczorek et al., 2013). Some corrections have been made to the model and are noted below.

The model solves a system of 5 equations that links 8 parameters expressed in spherical harmonics (degree l, order m): the topography (H_{lm}), geoid at the surface of the planet (G_{lm}), geoid at the base of the crust (Gc_{lm}), net acting load on the lithosphere (q_{lm}), tangential load potential (Ω_{lm}), flexure of the lithosphere (w_{lm}), crustal root variations (δc_{lm}), and internal lateral density variations ($\delta\rho_{lm}$). Given 3 constraints or assumptions, the system is evenly determined. To simplify the following equations, the mass-sheet approximation is used (see Wieczorek et al., 2013 and Broquet 2022 for more details).

The net load acting on the lithosphere can be shown to be equal to (e.g., Broquet & Wieczorek, 2019)

$$q_{lm} = g_0\rho_c(H_{lm} - G_{lm}) + g_m\Delta\rho(w_{lm} - \delta c_{lm} - Gc_{lm}) + g_M\delta\rho_{lm}M \quad \text{(A1)}$$

where $\Delta\rho = \rho_m - \rho_c$ is the density contrast across the crust-mantle interface; g_0, g_m, and g_M are the vertical gravitational acceleration at the surface, crust-mantle boundary and at the base of the internal load; and M is the thickness of the internal density anomaly. If the gravitational acceleration is assumed to be constant, our equation (A1) reduces to eq. (4) in Banerdt (1986). Assuming that internal density variations are located between M_t and M_b, and using the mass-sheet assumption, the geoid at the surface can be derived as (see also Wieczorek & Phillips, 1998),

$$G_{lm} = \frac{3}{\bar{\rho}(2l+1)} \left\{ \rho_c H_{lm} + \Delta\rho(w_{lm} - \delta c_{lm})\varphi^{l+2} + \delta c_{lm} \frac{R}{l+3} \left[\left(\frac{R - M_t}{R} \right)^{l+3} - \left(\frac{R - M_b}{R} \right)^{l+3} \right] \right\}.$$

(A2)

In this equation, $\varphi = (R - T_c)/R$. Similarly, the geoid at the base of the crust is given by

$$Gc_{lm} = \frac{3}{\bar{\rho}(2l+1)} \left\{ \rho_c H_{lm} \varphi^{l+1} + \Delta\rho(w_{lm} - \delta c_{lm})\varphi^3 + \delta c_{lm} \frac{R}{l+3} \left[\frac{\left(\frac{R - T_c}{R - M_t} \right)^{l+1} - (R - M_t)^3}{(R - T_c)R^2} - \frac{\left(\frac{R - T_c}{R - M_b} \right)^{l+1} - (R - M_b)^3}{(R - T_c)R^2} \right] \right\},$$

(A3)

Equation (A2) is similar to eq. (6) in Banerdt (1986), and minor corrections have been made to equation (A3), with respect to eq. (5) in Banerdt (1986), to properly reference the different interfaces at the base of the crust.

The tangential load potential has been derived by Banerdt (1986) as

$$\Omega_{lm} = \frac{v}{1-v} \rho_c g_0 T_e \frac{H_{lm}}{R} - \left[\rho_c g_m \left(\frac{v}{1-v} T_e - T_c \right) - \rho_m g_m max(T_e - T_c, 0) \right] \frac{w_{lm}}{R} - \frac{v}{1-v} \Delta\rho g_m max(T_e - T_c, 0) \frac{\delta c_{lm}}{R} - \frac{1}{2} \frac{v}{1-v} \delta\rho_{lm} g_m max(T_e - M_t, 0) \frac{min(M, T_e - M_t)}{R}.$$

(A4)

Equation (A4) has been modified to include lateral density variations at any arbitrary depth. We note that any internal density variations below the elastic lithosphere do not give rise to tangential loads, as these are assumed to be in the fluid mantle.

The flexure equation is obtained from Beuthe (2008)

$$w_{lm} = \frac{-R_e^4(\nabla + 1 - v)q_{lm} + R_e^4 \left(\frac{1}{1+\xi}(\nabla + 2) - 1 - v \right) \nabla\Omega_{lm}}{\eta D \nabla(\nabla + 2)^2 + \frac{R_e^2}{ET_e}(\nabla + 2)}$$

(A5)

where, $\nabla = -l(l+1)$ is the Laplacian, $D = ET_e^3/(12(1-v^2))$ is the bending rigidity of the shell, $\xi = 12R_e^2/T_e^2$, and $\eta = \xi/(1 + \xi)$. The flexure equation is slightly different from that derived in Banerdt (1986), with a correction that mostly affects the degree-1 terms (see Beuthe 2008).

Strains are computed using the flexure and the poloidal component of the tangential displacement, which is defined following Beuthe (2008) as

$$A_{lm} = \frac{1}{(1+\xi)(1-v^2)}(\nabla + 1 + v)(\nabla + 2)w_{lm} + w_{lm} + \frac{R_e^2 q_{lm}}{ET_e} - \frac{R_e^2}{(1+\xi)ET_e}\big(\nabla - \xi(1+v)\big)\Omega_{lm}$$

(A6)

From equations (A5) and (A6), one can derive the 6 components of the strain tensor (e.g., eq. 12 in Beuthe, 2008).

S3. Fitting the strain magnitude at Hesperia Planum.

We make use of the best-fit plume location and determine what parameters best reproduce the observed strain magnitude. To facilitate viewing the three-dimensional parameter space, we have fixed one parameter for each panel of Figure S2. We estimate a residual strain as the difference between the observed and predicted areal strain, both averaged over our restricted investigated region. Where the model best matches observations, the residual strain should be approximately $1.47–1.76\times10^{-3}$, which is the strain attributed to global contraction (section 3.3 in the main text).

In our models, there is roughly a one-to-one tradeoff between the density contrast and aspect ratio of the plume head (Figure S2A), which both control the mass and load of the plume. Decreasing the elastic thickness increases the residual strain (S2B), which is the result of our loading model approaching isostatic equilibrium ($T_e = 0$), where stresses and strains are minimum.

In order to best reproduce the observed strain magnitude and when flood lava loading is negligible, the plume-head density contrast should be at least -25 kg m^{-3} (thermal anomaly of about 215 K), the aspect ratio must be greater than 0.11, and any elastic thickness can satisfy the data. When accounting for the presence of the flood basalt, with an initial thickness of 500 m, less strain should originate from the plume-head. The density contrast and aspect ratio are both reduced, with minimum allowed values down to -10 kg m^{-3} and 0.09, respectively (Figure S2).

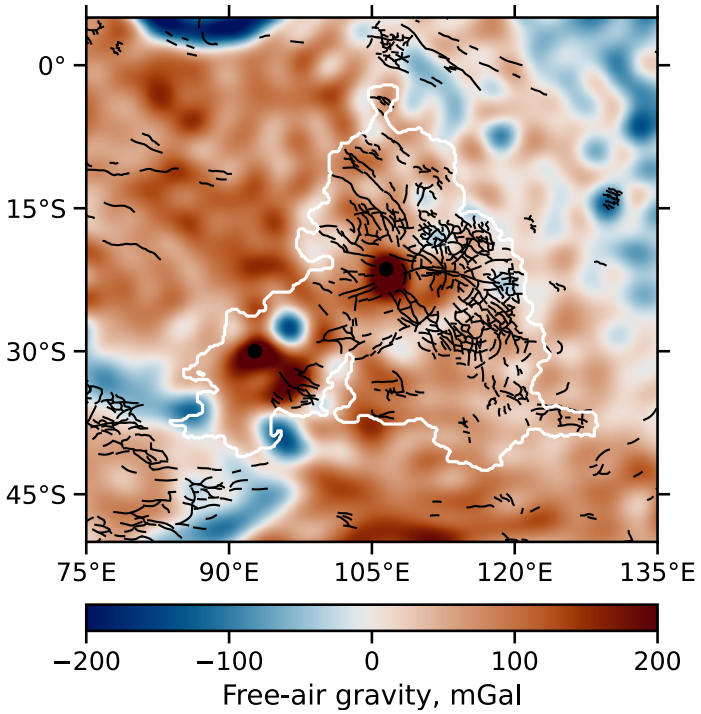

Figure S1: Gravity field at Hesperia Planum. Free-air gravity at Hesperia Planum based on the model of Genova et al. (2016). For geologic context, the images are annotated with a white contour of Hesperia Planum, black lines for compressive tectonic features and black dots for Tyrrhena (106°E -21°N) and Hadriaca (93°E -30°N) Montes.

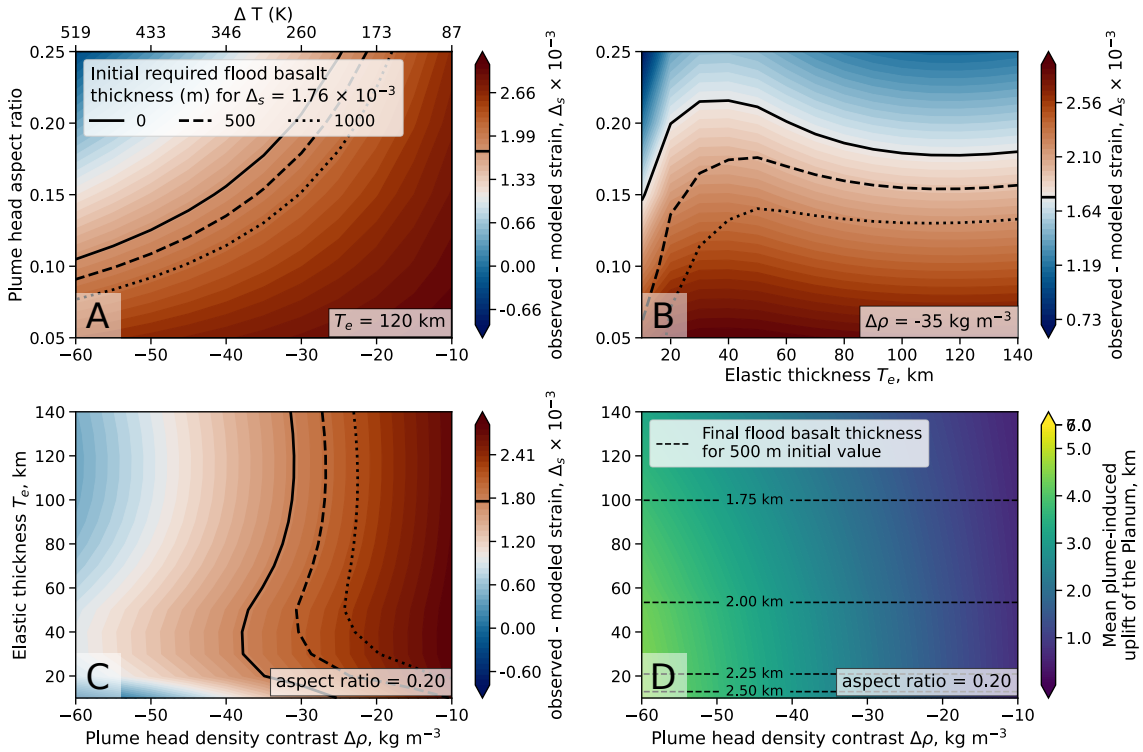

Figure S2: Strain magnitude and displacement at Hesperia Planum. (**A**) Residual strain (the difference between the observed strain of 3.20×10^{-3} and modeled areal strain) as a function of the density contrast (or temperature anomaly) and aspect ratio for an elastic thickness of 120 km. (**B**) Residual strain for different elastic and plume-head thicknesses for a density contrast of -35 kg m^{-3}. (**C**) Residual strain as a function of the density contrast and elastic thickness for an aspect ratio of 0.20. Black contours indicate where the residual strain is 1.76×10^{-3}, which is our estimate for the background Hesperian strain, for several initial thicknesses of the flood basalt. (**D**) Maximum predicted surface uplift for different elastic thickness and plume-head density contrast for an aspect ratio of 0.20. This plot is also annotated by the final flood basalt thickness depending on the elastic thickness and for an initial thickness of 500 m.

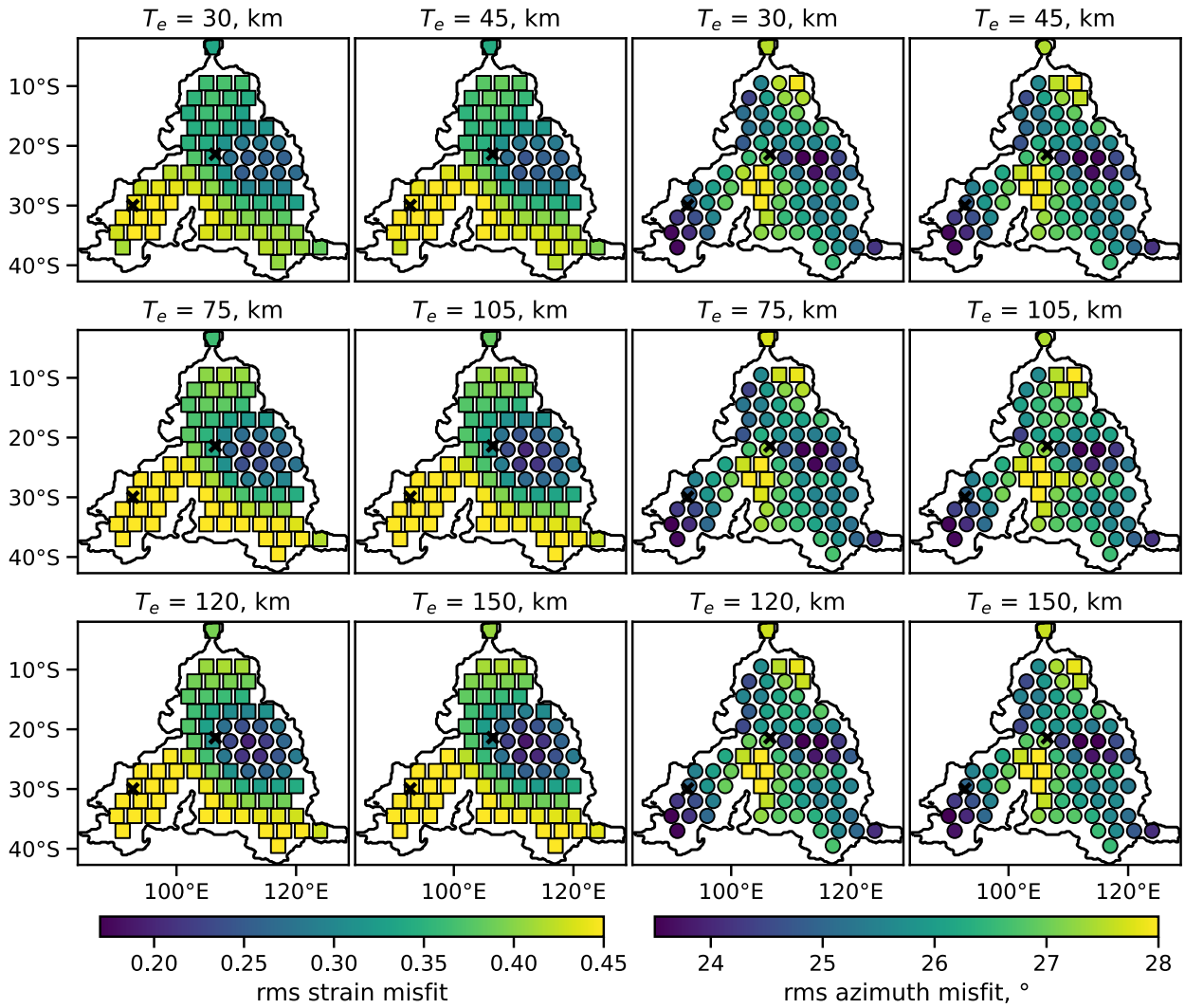

Figure S3: Mantle plume position and elastic thickness. Influence of the thickness of the elastic lithosphere on the RMS misfit between the observed and modeled strain concentration (2 leftmost columns) and azimuth (2 rightmost columns) as a function of the position the plume-head (colored markers). The plume-head radius, density, and aspect ratio were set to 700 km, -35 kg m^{-3}, and 0.20 respectively. Where the RMS misfit is lower than when using global gravity and topography (0.29) the location markers are dots, and are squares elsewhere. The black cross indicates the position of Tyrrhena and Hadriaca Montes.

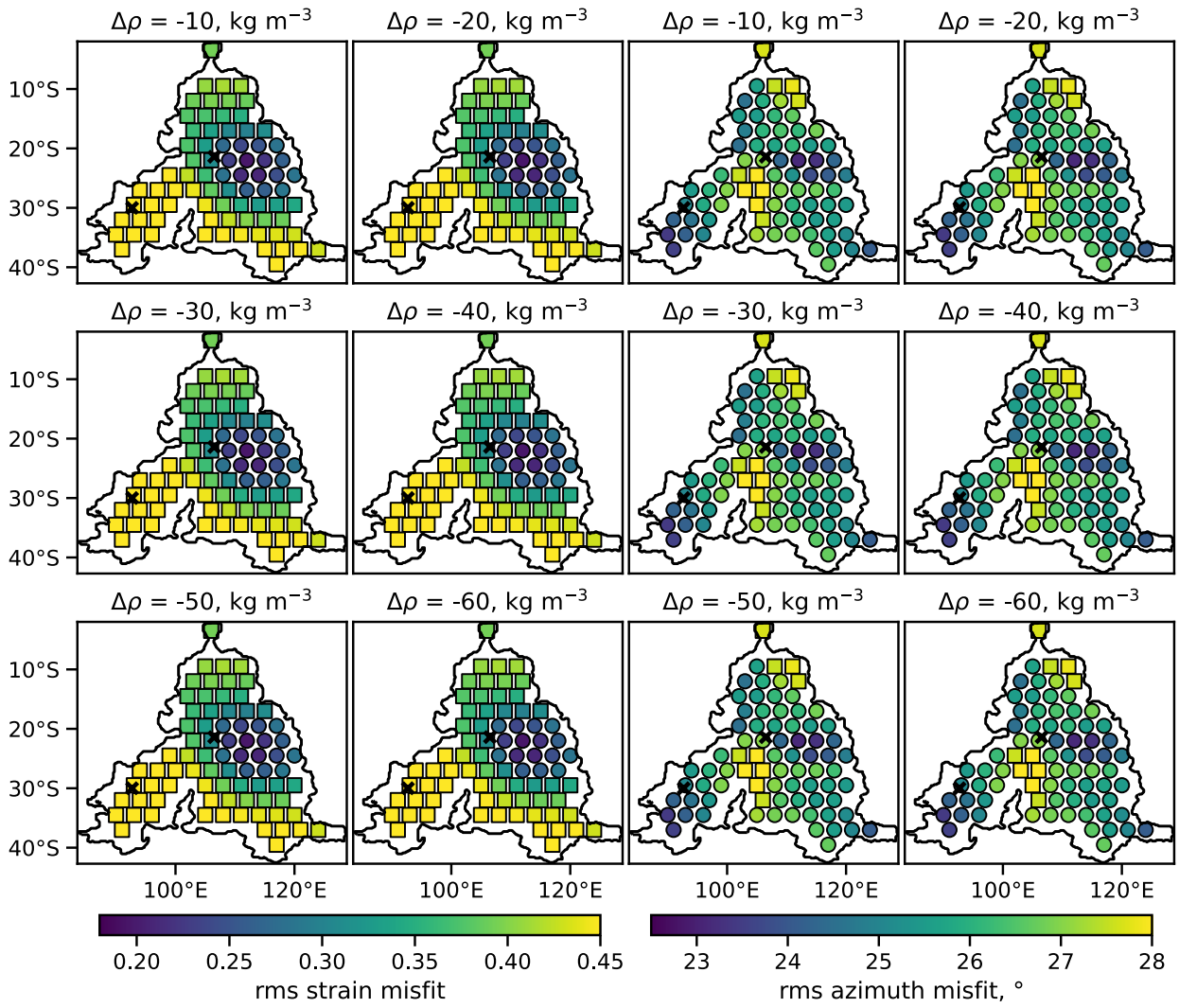

Figure S4: Mantle plume position and density contrast of the plume-head. Influence of the density contrast of the plume-head on the RMS misfit between the observed and modeled strain concentration (2 leftmost columns) and azimuth (2 rightmost columns) as a function of the position the plume-head (colored markers). The elastic thickness, plume-head radius and aspect ratio were set to 120 km, 700 km, and 0.20 respectively.

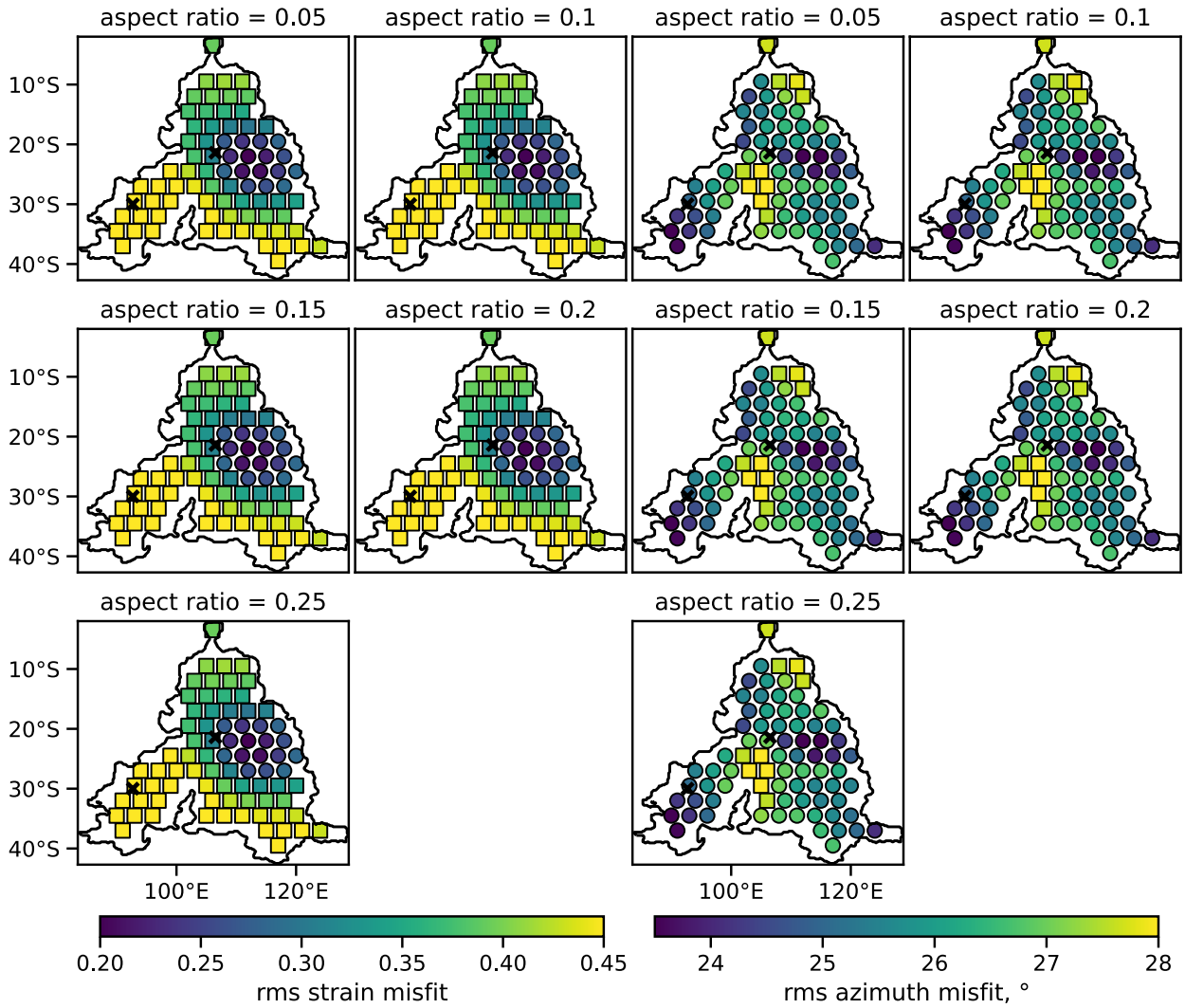

Figure S5: Mantle plume position and the aspect ratio of the plume-head. Influence of the aspect ratio of the plume-head on the RMS misfit between the observed and modeled strain concentration (2 leftmost columns) and azimuth (2 rightmost columns) as a function of the position the plume-head (colored markers). The elastic thickness, plume-head radius and density contrast were set to 120 km, 700 km, and -35 kg m^{-3}, respectively.

References

Banerdt, W. B. (1986). Support of long-wavelength loads on Venus and implications for internal structure. *Journal of Geophysical Research: Solid Earth*, *91*, 403– 419. https://doi.org/10.1029/JB091iB01p00403.

Broquet, A. (2022). AB-Ares/Displacement strain planet: Version 0.4.0. *Zenodo*. https://doi.org/10.5281/zenodo.5784417.

Beuthe, M. (2008). Thin elastic shells with variable thickness for lithospheric flexure of one-plate planets. *Geophysical Journal International*, *172*(2), 817–841. https://doi.org/10.1111/j.1365-246X.2007.03671.x.

Broquet, A., & Wieczorek, M. A. (2019). The gravitational signature of Martian volcanoes. *Journal of Geophysical Research: Planets*, *124*(8), 2054–2086. https://doi.org/10 .1029/2019JE005959.

Campbell, I. H., & Griffiths, R. W. (1990). Implications of mantle plume structure for the evolution of flood basalts. *Earth and Planetary Science Letters, 99*(1), 79–93. https://doi.org/10.1016/0012-821X(90)90072-6.

Genova, A., Goossens, S., Lemoine, F. G., Mazarico, E., Neumann, G. A., Smith, D. E., & Zuber, M. T. (2016). Seasonal and static gravity field of Mars from MGS, Mars Odyssey and MRO radio science. *Icarus*, *272*, 228–245. https://doi.org/10.1016/j.Icarus.2016.02.050.

Griffiths, R. W., & Campbell, I. H. (1991). Interaction of mantle plume heads with the Earth's surface and onset of small-scale convection. *Journal of Geophysical*

Research: Solid Earth, 96(B11), 18295–18310. https://doi.org/10.1029/91JB01897.

Plesa, A.-C., Padovan, S., Tosi, N., Breuer, D., Grott, M., Wieczorek, M. A., Spohn, T., Smrekar, S. E., & Banerdt, W. B. (2018). The thermal state and interior structure of Mars. *Geophysical Research Letters, 45*(22), 12,198–12,209. https://doi.org/10.1029/2018GL080728.

White, R. S., & McKenzie, D. (1995). Mantle plumes and flood basalts. *Journal of Geophysical Research: Solid Earth, 100*(B9), 17543–17585. https://doi.org/10.1029/ 95JB01585.

Wieczorek, M. A., Neumann, G. A., Nimmo, F., Kiefer, W. S., Jeffrey, T. G., Melosh, H. J., Phillips, R. J., Solomon, S. C., Andrews-Hanna, J. C., Asmar, S. W., Konopliv, A. S., Lemoine, F. G., Smith, D. E., Watkins, M. M., Williams, J. G., & Zuber, M. T. (2013). The crust of the Moon as seen by GRAIL. *Science*, *339*(6120), 671–675. https://doi.org/10.1126/science.1231530.

Wieczorek, M. A., & Phillips, R. J. (1998). Potential anomalies on a sphere: Applications to the thickness of the lunar crust. *Journal of Geophysical Research: Planets*, *103*(E1), 1715–1724. https://doi.org/10.1029/97JE03136.